Seasonal variation in size-resolved particle deposition and the effect of environmental conditions on dry deposition in a pine forest

Erin K. Boedicker[a], Holly M. DeBolt[a], Ryan Fulgam[a,*], Ethan W. Emerson[a,b], and Delphine K.

5   Farmer[a]

[a]Department of Chemistry, Colorado State University, Fort Collins, CO, USA; [b]Handix Scientific, Fort Collins,

CO, USA

* Now at Environmental Protection Agency, Durham, North Carolina, USA

10   *Correspondence to*: Delphine K. Farmer Delphine.Farmer@colostate.edu Department of Chemistry, Colorado

State University, 1301 Center Ave, Fort Collins, CO, 80523, USA.

Abstract

Dry deposition is a fundamental process that removes particles from the atmosphere, and therefore directly
controls their lifetime and total impact on air quality and radiative forcing. The processes influencing dry
15   deposition are poorly constrained in models. Seasonal changes in dry deposition remain uncertain due to the
lack of observations over multiple seasons. We present measurements of size-resolved sub-micron particle
deposition from a flux study that surveyed all four major seasons. Particle concentrations and therefore fluxes
were highest in the summer and lowest in the winter. Size-dependent deposition velocities in all seasons were
consistent with previously observed trends, however, our observations show a $130 \pm 60\%$ increase in wintertime
20   deposition velocity compared to the summer, which is not currently captured in size-resolved deposition
models. We explore the influence of scalar gradients and changes in environmental conditions as possible
drivers of this increase. We find that phoretic effects, such as thermophoresis, and the addition of snow to the
canopy had negligible impacts on our canopy level measurements. While turbophoresis impacted the observed
seasonal changes in size-resolved particle deposition velocity, it did not fully explain the observed differences
25   between the summer and winter. We suggest that the increase in deposition velocity is instead caused by
changes to the leaf-level conditions and physiology during the wintertime, which increase interception of
particles.

1   Introduction

30   Particles impact the quality of the air and radiative balance of Earth's atmosphere as a function of their size,
chemical composition, and lifetime. The lifetime of particles is controlled by their rate of removal. The two removal
pathways for particles from the atmosphere are wet deposition, which is the scavenging of particles and subsequent
removal by precipitation, and dry deposition, which is the removal of particles through interactions with terrestrial
and aquatic surfaces. Dry deposition of particles in the accumulation mode is currently the largest source of
35   uncertainty in global models in the prediction of concentrations of cloud condensation nucli and the prediction of
particle impacts on cloud albedo (Carslaw et al., 2013; Lee et al., 2012, 2013). Uncertainty in dry deposition
removal rates stem from both inaccuracy in current theoretical parameterizations and the limited spatial and
temporal coverage of measurements, especially over certain terrestrial surfaces during seasons other than
summertime. Understanding the removal of particles through dry deposition is critical for constraining particle
40   lifetime and therefore total impact in the atmosphere. While there have been major strides in quantifying and

understanding dry deposition, large gaps in our knowledge of underlying deposition mechanisms persist (Farmer et al., 2021; Saylor et al., 2019; Hicks et al., 2016; Pryor et al., 2008).

Several terms can be used to describe the biosphere-atmosphere exchange of particles. Particle flux describes the net exchange of particles and is strongly influenced by changes in particle concentration and size distribution in an environment. Environments exhibit seasonal changes in concentration and size distribution that can influence particle flux; this is easily observed in urban environments where local particle sources persist. During the winter in urban regions particle concentration and therefore flux often increase due to an increased use of heating systems (Casquero-Vera et al., 2022). In contrast, rural environments often see increases in particle flux during the summer due to the dominance of biogenic secondary organic aerosol. In the same way, size distribution changes can influence particle flux. For these reasons particle flux is ideal for identifying sources of particles within an environment. Exchange velocity (V_{ex}) is derived from the flux and is independent of the particle concentration, describing the vertical directional movement of particles in an environment. Both flux and V_{ex} follow the same sign convention where positive indicates upward movement, or emission, and negative indicates downward movement, or deposition. Deposition velocity (V_{dep}) describes the portion of exchange velocities that have a downward direction – using a positive sign for velocities directed downward towards biosphere surfaces– and defines how quickly particles are collected by the surface. Since these terms are independent of concentration and size distribution changes, their behavior should remain unchanged unless there are shifts in the underlying mechanisms driving these velocities.

The extent to which the mechanisms behind dry deposition velocity over terrestrial ecosystems vary with ecosystem properties or other seasonally varying parameters remains poorly constrained by observations. Few studies have presented either bulk aerosol deposition velocity (e.g. Zhai et al. 2019; Ahlm et al. 2010; Rannik et al. 2009; Suni et al. 2003) or size resolved deposition measurements across seasons (e.g. Petroff et al. 2018; Mammarella et al. 2011; Gallagher et al. 1992). These studies typically observe seasonal differences in both particle flux and deposition velocity and have raised several hypotheses regarding seasonality of particle dry deposition. In their study of cloud droplet deposition (3 – 31 µm), Gallagher et al. (1992) observed a reduction in deposition velocity during wintertime snow cover that they attributed to the addition of snow to the canopy thereby reducing overall surface roughness. In contrast, Mammarella et al. (2011) observed an increase in deposition velocity in the winter, while the fall and summer periods had the lowest deposition velocities. Mammerella et al. suggested wintertime enhancements in ultrafine (0.020 – 0.065 µm) particle deposition velocities were due to thermophoretic effects, and changes to other particle sizes were due to either turbophoretic effects or changes in the concentration of various modes in the seasonal distributions. Thermophoresis occurs when thermal gradients drive particles towards the collecting surface. When the air is warmer than the collecting surface the increased energy in the space above the surface drives collisions and interactions that propel particles away from each other and towards areas with smaller energy reservoirs, which in this case is the colder collecting surface. Turbophoresis is the movement of particles by gradients in turbulence. For this mechanism, increased turbulence in areas above the canopy and collecting surface drive particle collisions and interactions which in turn move particles away from the areas of high turbulence and towards regions of low turbulence. In this way both processes enhance the interaction time between the particle and the surface, therefore increasing the deposition velocity. Phoretic effects describe the effects of all scalar gradients, including thermophoresis and turbophoresis, and have been explored as contributors to deposition over snow and ice surfaces (Petroff and Zhang, 2010; Tammet et al., 2001). Turbophoresis in particular has been considered as a contributor to particle deposition in forests where trees create significant gradients in turbulence between the top of the canopy and the forest floor (Katul et al., 2010; Feng, 2008). Another seasonal factor that could impact dry deposition is the condition of the forest canopy or vegetation structure. Particle uptake by vegetation is a significant contributor to dry deposition (Pryor et al., 2017), and plant morphology and physiology impacts particle deposition (He et al., 2020; Räsänen et al., 2012, 2013). Changes to the canopy structures affect eddy penetration which could also impact turbophoresis. Seasonal changes in leaf-level conditions could therefore have significant impacts on dry deposition. The relative influence of each of these proposed mechanisms has not been critically evaluated, due to the limitations of available measurements, but they have been incorporated in some particle deposition models.

The objective of this work was to investigate seasonal variation in particle concentration and fluxes over a temperate pine forest from the Seasonal Particles in Forests Flux studY (SPiFFY) in 2016. We present general trends in

meteorology, particle concentration and distribution, and particle flux across the four seasons: winter, spring, summer, and fall. Additionally, we present seasonal trends in total and size-resolved particle deposition velocity compared to current resistance model parameters. This work explores the drivers of seasonal variations in particle deposition and presents new evidence for the addition of previously neglected mechanisms in dry deposition

95   modules as well as the inclusion of seasonally specific constants.

2   Methods

2.1   Site Description

The Seasonal Particles in Forests Flux studY (SPiFFY) was conducted at Manitou Experimental Forest Observatory

100   (MEFO) located within Manitou Experimental Forest in central Colorado, USA (39.1006°N, 105.0942°W). Four measurement campaigns were performed between 2015 and 2016, each representative of one of the major seasons: winter (February 1 – March 1, 2016), spring (April 15−May 15, 2016), summer (July 14−September 16, 2016), and fall (October 1−November 1, 2016). Manitou Experimental Forest is approximately 6760 ha of ponderosa pine, Douglas fir, mixed conifer, and aspen vegetation with an average canopy height of 16 m. Manitou Experimental

105   Forest elevation ranges from 2280 – 2840 m above sea level. The MEFO tower site is described in detail by Ortega et al. (2014). Measurements were made at the 30 m walk-up tower at MEFO, with instrumentation installed in an exterior trailer at the base of the tower. The footprint of the tower was dominated by Ponderosa pine trees reaching 16 m in height.

Fulgham et al. (2019) summarized the meteorology of the site across the four seasons during SPiFFY, which is

110   presented in **Figure 1** and **Table 1**. The friction velocity ($u*$) and sensible heat flux (H) followed the conventional diel cycles associated with increases in solar heating during the day, enhancing turbulence, and decreases at night (**Figure 1**). This trend is observed in all four seasons, with the summer and fall having the strongest increase in sensible heat during the day. Friction velocities were comparable across seasons; however, the winter did exhibit higher turbulence during nighttime periods than other seasons. Further details of the site set up and these trends can

115   be found in Supplemental **Figure S1 & S2**.

2.2   Instrumentation

Size-resolved particle concentrations were measured using an Ultra-High Sensitivity Aerosol Spectrometer (UHSAS; DMT Inc., Longmont, CO; Cai et al. 2008). The UHSAS had a 10 Hz time resolution and counted

120   particles in 99 size bins (0.06 – 1 µm). The data was re-binned during analysis to 10 size bins, and data from 0.06 – 0.089 µm was not included in the analysis due to the presence of noise that caused irregular and severe fluctuations in the signal of that size range. Calibrations were run at the beginning of each deployment using NIST standard polystyrene latex spheres (60, 150, 300, 600, and 900 nm mobility diameter). System zeros were run using a HEPA filter and switch installed at the front of the main line. The inlet set-up for the measurements consisted of a 28.98 m

125   (ID: 7.14 mm, OD: 9.53 mm) copper line installed 25 m above ground level on the tower and was co-located with the sonic anemometer. A cone with metal mesh to keep out bugs and debris was affixed to the front of the inlet. Flow through the main line was maintained at ~20 L/min (Re ≈ 3900; residence time of 3.5 s in the main line) using a backing pump and mass flow controller. Inside the trailer, a 3.05 m line reduced to ID: 4.83 mm (OD: 6.35 mm), and the UHSAS sampled off the main line at 60 mL/min through its internal conductive silicone tubing (OD: 3.2

130   mm) (**Figure S1**). Particle loss in the main line calculated using the method described by Von der Weiden et al. (2009) was determined to be negligible (<5%).

Two different sonic anemometers were used during the campaign to measure three-dimensional wind speed and temperature. For the winter, spring, and summer periods (February 1 – August 5, 2016), we used a CSAT3 sonic anemometer (Campbell Scientific, Logan, UT). Inlet offsets from the CSAT were $x = 20$ cm, $y = 40$ cm, $z = 10$ cm.

135   The fall measurements (October 1−November 1, 2016) used a SATI-series K-style sonic anemometer (Applied Technologies Inc., Boulder, CO). Inlet offsets from the SATI were $x = 0$ cm, $y = 0$ cm, $z = 60$. Both anemometers were set to record data at 10 Hz time resolution. Data from the CSAT3/SATI and UHSAS were logged on separate computers and the timestamps were synched to an online time server. Any observed clock drifts in the data were handled in post processing.

140
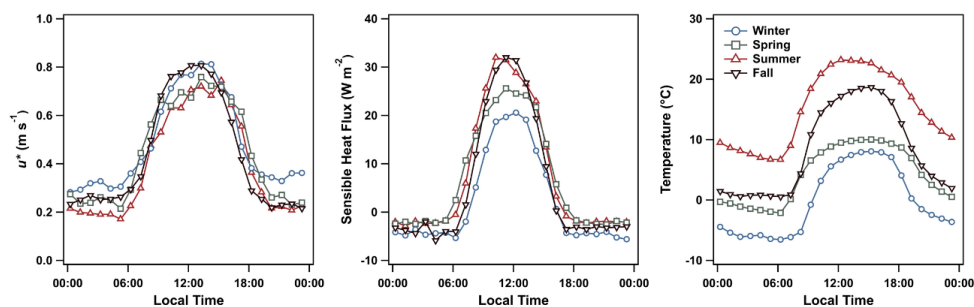
Figure 1: Average diel cycle for friction velocity ($u*$), sensible heat flux (H), and air temperature of each season. Each point represents an hourly median value.

145   **Table 1**: Seasonal environmental daytime conditions, originally published by Fulgham et al. (2019).

	Friction Velocity (m/s)	Wind Speed (m/s)	Temperature (°C)	Relative Humidity (%)
	$\mu \pm \sigma$ (min − max)	$\mu \pm \sigma$ (min − max)	$\mu \pm \sigma$ (min − max)	$\mu \pm \sigma$ (min − max)
Winter	0.5 ± 0.3 (0.025 − 1.6)	3.5 ± 2 (0.25 − 11)	7 ± 5 (-7.0 − 16)	27 ± 10 (8.0 − 88)
Spring	0.4 ± 0.3 (0.030 − 1.6)	3.6 ± 2 (0.0 − 18)	10 ± 6 (-3.7 − 21)	40 ± 20 (0.0 − 93)
Summer	0.4 ± 0.3 (0.030 − 1.5)	3.0 ± 1 (0.0 − 10)	23 ± 4 (11 − 29)	33 ± 20 (0.0 − 86)
Fall	0.4 ± 0.3 (0.005 − 1.7)	3.4 ± 2 (0.0 − 11)	15 ± 4 (0.5 − 23)	25 ± 10 (0.0 − 92)

2.3 Eddy Covariance Measurements

150 Surface-atmosphere exchange was measured using eddy covariance flux techniques. The vertical flux (F_c) in this technique is determined by the covariance of the vertical wind speed (w) and a scalar (c; particle concentration):

$$F_c = \overline{w'c'} = \frac{1}{N} \sum_{i=0}^{N} (c_i - \bar{c})(w_i - \bar{w}) \tag{1}$$

where N is the number of points, w_i and c_i are the instantaneous measurements of the vertical windspeed and particle concentration respectively, and $\bar{w}$ and $\bar{c}$ are the mean values. We used a flux averaging time interval of 30-min.

155 Deposition velocity can be derived from the vertical flux and the mean concentration over a given period.

$$F_c = -V_{dep}\,\bar{c} \tag{2}$$

Using this notation, a positive V_{dep} corresponds to deposition and a negative V_{dep} indicates an emission. We treat the positive and negative fluxes as two separate processes following uneven distribution of positive and negative fluxes around zero (**Figure S3**). Only negative fluxes were used to derive deposition velocities, consistent with other

160 particle flux studies (Emerson et al., 2020; Lavi et al., 2013). Pryor et al. (2013) identified drivers of positive fluxes in a pine forest, which gives additional support to the separation of positive and negative fluxes in the calculation of deposition velocities (V_{dep}). Additionally, the variability in some of the seasonal measurements was high, resulting in means either at the edge or outside the 25th to 75th confidence intervals; we thus use the medians of the deposition velocity data to investigate changes between seasons.

165 ### 2.3.1 Data Treatment and Quality Control

Several quality controls were enforced on the data based on u^*, stationarity, and precipitation events. We also removed data taken during exceptional events. For example, during the fall campaign period, several prescribed burns were carried out in an area adjacent to MEFO. We exclude particle flux data from time periods in which CO

170 concentration was elevated (> 3800 ppb), which resulted in the removal of data from 10th October. Data that did not meet the following requirements for u^*, stationarity, and precipitation quality control were rejected:

1. Periods in which turbulence was not well developed, defined by a friction velocity (u^*) < 0.14 m/s, were excluded (Papale et al., 2006; Reichstein et al., 2005).
2. Measurement periods in which the flux was not in steady state, as determined by a stationarity test, were

175   excluded as they fail the assumptions of the eddy covariance method. A stationarity test compares 5-min fluxes to the full 30-min flux to ensure that the fluxes do not vary during the period of interest (Foken and Wichura, 1996). A period is considered to have stationarity if the 5-min periods do not deviate from the 30-min period by more than 30%, and the following criterion is met:

$$0.7 < \frac{\overline{\langle w'c'\rangle}_{5min}}{\overline{\langle w'c'\rangle}_{30min}} < 1.3 \tag{3}$$

180 3. Precipitation events were excluded from this analysis, as they can affect the signal of the sonic anemometer and distort the measured flux. A total of 24 precipitation events occurred, 3 in the winter, 12 in the spring, 9 in the summer, and zero in the fall.

These filters resulted in 241, 180, 305, and 363 flux periods for winter, spring, summer, and fall respectively. Results of each test and the number of flux periods impacted is summarized in **Table 2** (**Figure S3**).

185

Table 2: Summary of quality control tests for the SPiFFY campaign. Number of flux periods that did not meet the quality control factor listed as well as the percent of the total available measurements that did not meet the standard, are presented for each test and each season. The original number of measurement periods is listed under the season headers, and the number of flux periods retained are listed in the final row.

	Winter (N=858)	Spring (N=1001)	Summer (N=1330)	Fall (N=1433)
$u*$	76 (9%)	141 (14%)	198 (15%)	231 (16%)
Stationarity	513 (60%)	722 (72%)	965 (73%)	1019 (71%)
Precipitation	96 (11%)	279 (28%)	0 (0%)	12 (0.01%)
Accepted Flux Periods	**241 (28%)**	**180 (18%)**	**305 (23%)**	**363 (25%)**

2.3.2 Corrections

A single point storage correction was applied to the data in order to account for the difference in turbulent flux bellow the measurement height (Rannik et al., 2009).

$$F_{storage} = \int_0^{z_r} \frac{\delta \bar{c}}{\delta t} \, dz \approx \frac{\overline{c(t+\Delta T)} - \overline{c(t)}}{\Delta T} \tag{4}$$

This storage correction resulted in a < 1% change in the total flux in all four seasons.

Additionally, a two-dimensional rotation of windspeed in three axes corrected for the sonic anemometer not being mounted with a perfect level over the footprint (Wilczak et al., 2001; Massman, 2000).

2.3.3 Signal-to-Noise and Flux Uncertainty

To account for uncertainty in calculated flux measurements, we considered the signal-to-noise ratio of the UHSAS as well as flux uncertainty from instrument noise, counting statistics, and the covariance measurement. The signal-to-noise ratio of the UHSAS number concentration measurements is defined as the ratio between the mean concentration (μ) of a period and the standard deviation of the instrument signal during a system zero (σ_{zero}). A system zero is defined as a measurement period in which a HEPA filter is placed in front of the inlet. Here an adjacent period to the system zero was used to calculate the signal-to-noise ratio in each season (**Figure S4**).

$$SNR = \frac{\mu}{\sigma_{zero}} \tag{5}$$

Contribution of instrument noise to the flux uncertainty (δF_{noise}) was determined using the method described by Billesbach (2011). In this method it is assumed that the contribution of instrument noise to the total uncertainty is the covariance when the correlation coefficient is minimized, which is achieved by randomizing the time sequence of the scalar, or particle concentration.

$$\delta F_{noise} = \frac{1}{M} \sum_{i,j=1}^{M} w'(t_i) \, c'(t_j) \tag{6}$$

where M is the number of measurements in the interval, w' and c' are the deviations from the mean vertical windspeed and concentration, and i and j are the time indices.

The uncertainty in the flux from counting discrete particles (ΔF_N) is calculated using the cumulative number of particles (N), along with the mean concentration ($\bar{c}$), and the variance of the vertical velocity (σ_w) during a flux period (Fairall, 1984).

$$\Delta F_N = \frac{\sigma_w \bar{c}}{\sqrt{N}} \tag{7}$$

Finally, the uncertainty in the covariance is quantified here using the method outlined by Finkelstein and Sims (2001). Estimation of the random error comes from the calculation of variance of a covariance when the two

variables, here vertical windspeed and particle concentration, are lagged at unrealistic time scales (50 – 60s). Finkelstein and Sims (2001) outline the following parameterization for the variance of the covariance (σ^2):

$$\sigma^2 = \frac{1}{M} \left[\sum_{i=-m}^{m} \sigma_{x,x}^2(i)\, \sigma_{y,y}^2(i) + \sum_{i=-m}^{m} \sigma_{x,y}^2(i)\, \sigma_{y,x}^2(i) \right] \tag{8}$$

225   where M is the number of measurements in a flux period, $\sigma_{x,x}^2$ and $\sigma_{y,y}^2$ are the variance of the two variables, $\sigma_{x,y}^2$ and $\sigma_{y,x}^2$ are the estimated covariances of the two variables, and m is number of samples used to captures the integral time scale (m = 200, 20s of 10 Hz data). The auto- ($\sigma_{x,x}^2$) and cross-covariance ($\sigma_{x,y}^2$) is computed for a lag (h) by:

$$\sigma_{x,x}^2(h) = \frac{1}{M} \sum_{i=1}^{M-h} (x_t - \bar{x})(x_{t+h} - \bar{x}) \tag{9}$$

$$\sigma_{x,y}^2(h) = \frac{1}{M} \sum_{i=1}^{M-h} (x_t - \bar{x})(y_{t+h} - \bar{y}) \tag{10}$$

The subsequent uncertainty in the covariance ($\sigma_{w'N'}$) ranged from 30 – 80 # cm^{-2} s^{-1}. We also evaluated the time-
230   lagged covariance spectra for each flux period out to 50s to attempt and identify the time lag between the vertical windspeed and particle concentration measurements. However, the determination of a time lag by cross covariance is problematic for data limited by counting statistics (Langford et al., 2015) so a fixed lag time of 3.5 s was used based off the flow through the inlet line. We acknowledge that the use of a fixed lag time can lead to flux underestimation as it does not capture changes in the system over time. For all the calculations outlined above, some
235   variable notation has been changed from the original source in order to have consistent references in this work. Results of the error analysis are summarized in **Table 3**. The instrumental and random noise were both within the measured variation of the particle fluxes, however, the uncertainty from counting discrete particles exceeded the measured variation. This indicates that the uncertainty from counting is the overwhelming contributor to uncertainty in these flux measurements.

240   **Table 3:** Summary of uncertainty and LOD for total particle flux measurements during SPiFFY

	Winter	Spring	Summer	Fall
|Total Flux| ($\mu \pm \sigma$; # cm^{-2} s^{-1})	(2 ± 70)	(60 ± 100)	(50 ± 100)	(20 ± 100)
SNR	100	200	300	300
δF_{noise} (# cm^{-2} s^{-1})	20	30	30	20
ΔF_N (# cm^{-2} s^{-1})	800	2000	2000	1000
$\sigma_{w'N'}$ (# cm^{-2} s^{-1})	30	80	70	60
$\overline{LOD_{season}}$ (# cm^{-2} s^{-1})	8	40	20	20

2.3.4 Flux Limit of Detection

245 Limits of detection for individual flux periods (LOD_i) were first calculated considering random error using the method from Langford et al. (2015):

$$LOD_i = \alpha\, RE_i \tag{11}$$

with α being the specified confidence interval ($\alpha = 3$ was used for the 99th percentile in this work), and RE_i representing the random error of the flux period from the Finkelstein and Sims (2001) calculation above ($\sigma_{w'N'}$).

250 Time-resolved limits of detection were used to calculate an average limit of detection for each season, LOD_{season}.

$$\overline{LOD_{season}} = \frac{1}{N}\sqrt{\sum_{i=1}^{N} LOD_i^2} \tag{12}$$

For this project, the average limits of detection for particle flux measurements using this method were 8 (winter), 40 (spring), 20 (summer), and 20 (fall) # cm^{-2} s^{-1}. No flux periods were excluded based on comparison to $\overline{LOD}_{season}$ or time dependent LOD_i values as they still provide useful information when averaged (Langford et al., 2015). These

255 numbers are high compared to an LOD calculated through flux analysis on zero periods, which resulted in $\overline{LOD}_{zero}$ of 4 # cm^{-2} s^{-1} for both the winter and fall. While the $\overline{LOD}_{zero}$ needs further investigation if it is to be verified because it requires the attachment of a HEPA filter to the front of the inlet, which could change the turbulent dampening through the inlet and therefore require spectral correction before use. However, the large difference between $\overline{LOD}_{season}$ and $\overline{LOD}_{zero}$ indicates a need for the critical evaluation of LOD calculation methods for flux

260 measurements in the future.

2.3.5 Spectral Analysis

The UHSAS and other similar optical particle instruments have been previously used for eddy-covariance measurements, and their measurements have been validated using spectral analysis (Petroff et al., 2018; Deventer et

265 al., 2015). Here, we use spectral analysis to investigate and validate the measurements. Frequency weighted dimensionless cospectra of vertical wind speed and particle concentration followed the sensible heat, and the inertial subrange (f $^{-4/3}$) predicted by Kolmogorov theory is observed for each season between 0.01 and 5 Hz (**Figure 2**). **Figure 2** provides example cospectra for a 30-minute period from each season during the day where $u* \geq 1$ m s^{-1} to reduce noise caused by low turbulence. Stability during the periods were -0.03, -0.04, -0.10, and -0.04 for the winter,

270 spring, summer, and fall.
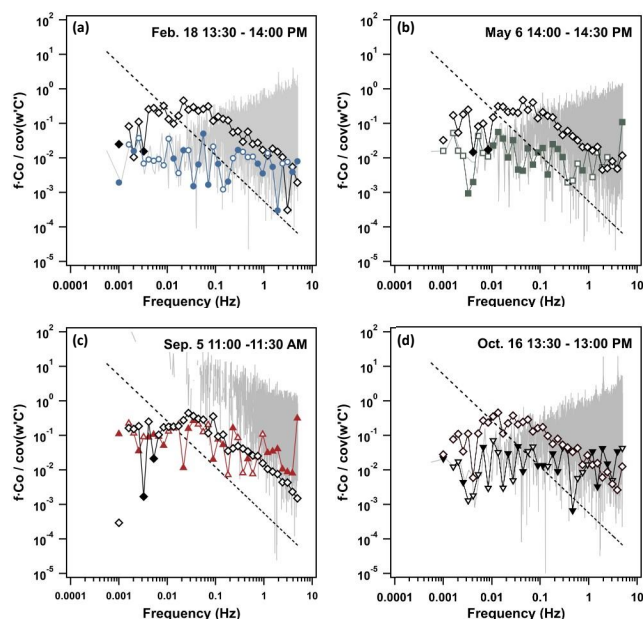
Figure 2: Frequency weighted dimensionless cospectral density of particle concentration (wC, color) and temperature (wT, black diamonds) with vertical wind speed for a representative 30-minute period for each of the four seasons. Individual data points are medians from 40 evenly spaced logarithmic bins, with open points representing positive data and closed points representing negative data that have been forced positive. The cospectra are presented for the (a) winter (blue circles), (b) spring (green squares), (c) summer (red upward triangles), and (d) fall (dark brown downward triangles). Raw wC cospectra are shown in light grey in the background and the inertial subrange ($f^{-4/3}$) is shown with the dashed line.

2.4 Deposition and Leaf Level Modeling

2.4.1 Deposition Models

We used the single layer resistance model from Emerson et al. (2020), which is based on the models presented by Zhang et al. (2001) and Slinn (1982), and aspects of the multi-layer model proposed by Katul et al. (2010) to investigate the roles of different mechanisms in controlling measured deposition velocities. The full parameterization of Emerson et al. (2020) along with the relevant parameterizations from Katul et al. (2010) are in **Appendix A**. We integrated the work of Katul et al. (2010) into the deposition velocity framework of Emerson et al. (2020) in order to investigate the impact of turbophoresis on particle deposition. Following Zhang and Slinn, the Emerson et al. (2020) framework is based on the gravitational settling velocity (V_g), the aerodynamic resistance (R_a), and the surface resistance (R_s).

$$V_d(d_p) = V_g(d_p) + \frac{1}{R_a + R_s} \tag{13}$$

We then incorporated the term developed by Katul et al. (2010) describing the collection efficiency of turbophoresis (E_{turbo}) into the surface resistance parameterization (R_s) from the Emerson et al. (2020) model by adding it in series to the collection efficiencies of Brownian diffusion processes (E_b), impaction (E_{im}), and interception (E_{in}) (Eq. 14).

$$R_s = \frac{1}{\varepsilon_0\, u^*\, (E_b + E_{im} + E_{in} + \boldsymbol{E_{turbo}})\, R_1} \tag{14}$$

295     $E_{turbo} = \frac{\tau_p}{1+\frac{\tau_p}{\tau}} \left(\frac{\sigma_w^2}{\pi\, b\, \eta} \right)$ (15)

The new surface resistance relies on the previously listed collection efficiencies, u^*, and the bounce correction (R_1) along with the empirical constant $\varepsilon_0 = 3$. E_{turbo} is dependent on the particle relaxation time (τ_p), Lagrangian turbulent timescale (τ), the standard deviation of the vertical velocity (σ_w), the thickness of the viscous sublayer for the vertical velocity variance (b), which can range from $5 < b < 50$, and the kinematic viscosity of air (η). In the

300   parameterization for E_{turbo}, the particle relaxation time (τ_p) is the size dependent term (**Appendix A**). While we were able to use measured values for σ_w and in the calculation of the Lagrangian turbulent timescale, these values can be approximated using u^*. Standard deviation of the vertical velocity trends linearly with u^*, with an acceptable approximation being $\sigma_w \approx 1.0\, u^* - 1.2\, u^*$ (Finnigan, 2000). Data from all four measurement periods of the SPiFFY campaign had a relationship of $\sigma_w \approx 1.1\, u^*$ (**Figure S5**). Additionally, the Lagrangian turbulent timescale

305   can be approximated by $\tau \approx (0.3\, u^*)\, /\, (1.1\, u^*)^2$. This approximation relies on the σ_w/u^* relationship from before as well as $u^*/\overline{U} \approx 0.3$ (Poggi et al., 2004; Finnigan, 2000), which we were also able to validate using the SPiFFY data (**Figure S6**).

2.4.2   Leaf Level Energy Balance and Thermophoretic Settling Velocity

310   We used a simple leaf energy balance to explore leaf effects on particle deposition. The energy balance calculations were based on equations outlined by Monteith (1990), Sridhar and Elliott (2002), and Jones (2014). We used the open-source single point leaf energy balance framework developed by Kevin Tu (http://landflux.org/Tools.php) to help structure the energy balance. We adapted these equations and frameworks to work with real time meteorology data reported by the U.S. Forest Service (Frank et al., 2021) along with sonic anemometer data collected during the

315   campaign periods. A full description of the leaf energy balance calculation is in **Appendix B**.

Thermophoretic settling velocity was calculated following Salthammer et al. (2011) and Hinds (1999). This velocity was then integrated into the Emerson et al. (2020) deposition model (**Appendix B**).

3   Results and Discussion
3.1   Seasonal trends in particle fluxes and concentrations

320

Total (0.08–1 µm) particle concentration (# cm^{-3}), flux (# cm^{-2} s^{-1}), and exchange velocity (V_{ex}, cm s^{-1}) all exhibited distinct diel cycles (**Figure 3, Figure S7**). The flux and V_{ex} magnitude peak in the middle of the day due to increased turbulence (see u^* in **Figure 1**), while particle number concentration peaks at night and decreases during the day as the boundary layer grows and mixes with larger volumes. Daytime fluxes were largest in the summer and spring

325   measurement periods, with nighttime fluxes being comparable across all four seasons. Flux measurements were dominated by downward fluxes in all seasons, except the winter, resulting in negatively skewed flux data (**Figure S3**).

As discussed in the introduction, particle concentration and size distribution can impact the direction and magnitude of particle fluxes. Particle concentrations were highest in the summer and lowest in the winter, providing a partial

330   explanation for the larger particle fluxes in summer versus winter. As exchange and deposition velocities are independent of concentration, seasonal shifts in size distribution could potentially account for the observed seasonality in these values. However, no major changes in the average size distribution occurred between seasons (**Figure 3**). Daytime count median diameters were 128 ± 8, 140 ± 20, 140 ± 10, and 130 ± 10 nm for the winter, spring, summer, and fall, respectively. These count median diameters did not change substantially at night (**Figure**

335   **S8, Table S1**). Particle distributions did not change between periods of positive and negative flux (**Figure S9, Table S2**). This consistency in the distributions indicates that changes in total particle exchange velocities are not attributable to seasonal shifts in size distribution.
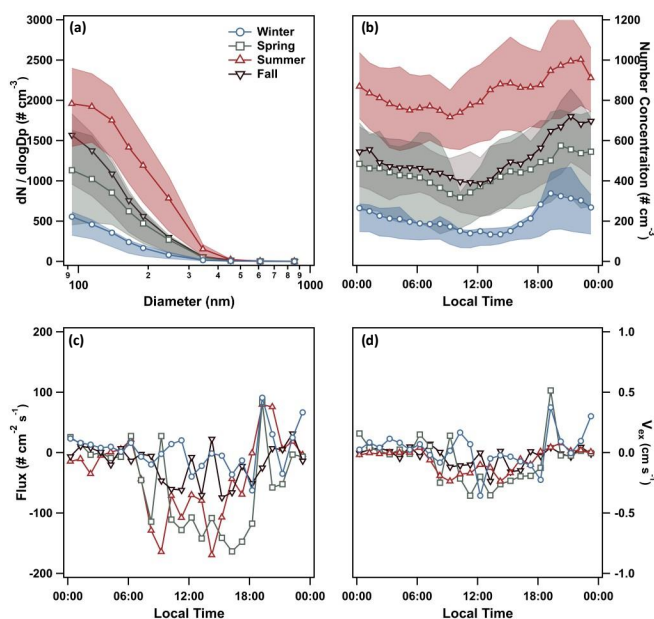
Figure 3: (a) Average daytime size distribution (dN/dlogDp) of particles for each season, with the 25th to 75th
340 confidence intervals shaded, as well as diel trends of hourly mean (b) total number concentration (also with the 25th
to 75th confidence intervals shaded), (c) flux, and (d) exchange velocity (V_{ex}) across seasons.

### 3.2 Measured and modeled seasonal trends in particle dry deposition

345 As noted above, we segregate the downward flux periods from periods in which upward fluxes occurred and used
these downward fluxes and their associate particle number concentrations to calculate deposition velocity, V_{dep}. Our
sign convention now switches to give positive velocities for V_{dep}. Deposition velocity for all particles measured
followed the diel trend of both friction velocity and sensible heat flux, with peak values occurring around noon
(**Figure 4**, **Figure S10**). Additionally, size-dependent deposition velocities in each season followed trends
350 previously observed in needleleaf forests (Lavi et al., 2013; Mammarella et al., 2011; Vong et al., 2010; Grönholm
et al., 2009a; GröNholm et al., 2007; Gallagher et al., 1997; Lorenz and Murphy, 1989). Binned deposition velocity
from all seasons had a strong linear relationship with friction velocity (**Figure 5**); this relationship was present in all
size ranges measured during the study with larger particles having bigger slopes (**Figure S11, Table S3**). This trend
is consistent with other particle deposition studies (Petroff et al., 2018; GröNholm et al., 2007).

355 While total deposition velocity did not vary significantly between seasons, the size-dependent deposition velocity in
the winter was greater than in the spring, summer, and fall. The enhancement of winter deposition relative to
summer was the largest and ranged from 23 – 202% (130 ± 60%) depending on particle size, with particles less than
0.35 µm having the largest enhancement. This enhancement decreased when deposition was normalized by $u*$,
ranging from 17 to 145 % (80 ± 40%), but was still significant based on t-tests of the size-dependent data (only the
360 0.505 – 0.711 µm range did not show significant difference). Wintertime enhancement of particle dry deposition
velocities has been observed in two other particle deposition studies. First, Suni et al. (2003) compiled six years
(1996 - 2001) of particle flux measurements (total particle number from 0.014 - 3 µm) over a Scots pine forest in
Hyytiälä, Finland, from 1996 to 2001. They hypothesized that the larger wintertime bulk deposition was a result of a
larger presence of small particles (< 0.10 µm) having larger deposition velocities, that when included in the
365 integrated total deposition velocity increased wintertime measurement. Second, Rannik et al. (2009) presented
particle flux measurements from the same site as Suni et al. (2003) but for 2000 to 2007. In contrast to Suni et al.,

Rannik et al. (2009) noted the same increase in wintertime deposition, but found that the number of nucleation days – on which small particles would dominate – was lowest in the winter. Additionally the continued analysis by Mammarella et al. (2011), indicated that the seasonal changes in geometric mean diameter were inadequate to cause

370   the increased winter deposition rates. Similar to our observations, Mammarella et al. (2011) found that size-dependent deposition velocities were significantly higher in winter than other seasons. That work concluded that the observed seasonal dependence of the dry deposition was driven by bi-modal distributions in the wintertime.

We investigated the cause of the wintertime increase in deposition during SPiFFY by comparing our results to the resistance model from Emerson et al. (2020), which is based on the work of Zhang et al. (2001) and Slinn (1982).

375   This model framework was chosen as the base comparison because of its wide use in chemical transport and climate models, including GLOMAP and GEOS-Chem, as well as its ability to assess the roles of Brownian motion, gravitational settling, interception, and impaction. Using measured values $u*$, windspeed, temperature, and stability function, we evaluated the ability of the Emerson et al. (2020) model to capture seasonal variation in both total and size-dependent dry deposition (**Figure 6**). While the model accurately captured the diel trends for the summer data,

380   there was a clear systematic underestimation of deposition in the other seasons. The largest underestimation was in the winter, when the predicted deposition was ~90% lower than the measured values (**Figure S12**). The size-resolved model predictions clearly disagreed with the measured winter deposition in every size bin. To resolve this disagreement we investigated additional mechanisms that are not currently accounted for in the Emerson et al. (2020) parameterization. Additionally, we explored possible seasonal dependencies for terms that are currently

385   considered, but not parameterized to be seasonally dependent (**Section 3.3**).
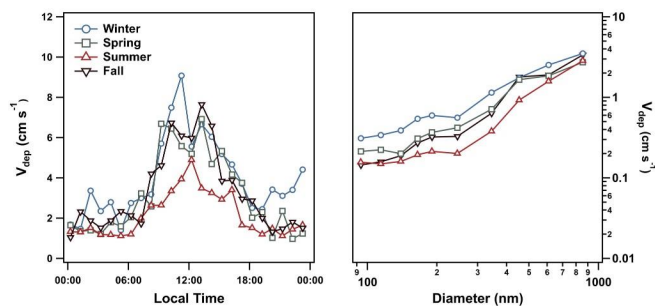
Figure 4: Diel cycle of median total particle dry deposition (left), and median size-dependent dry deposition for each season (right).
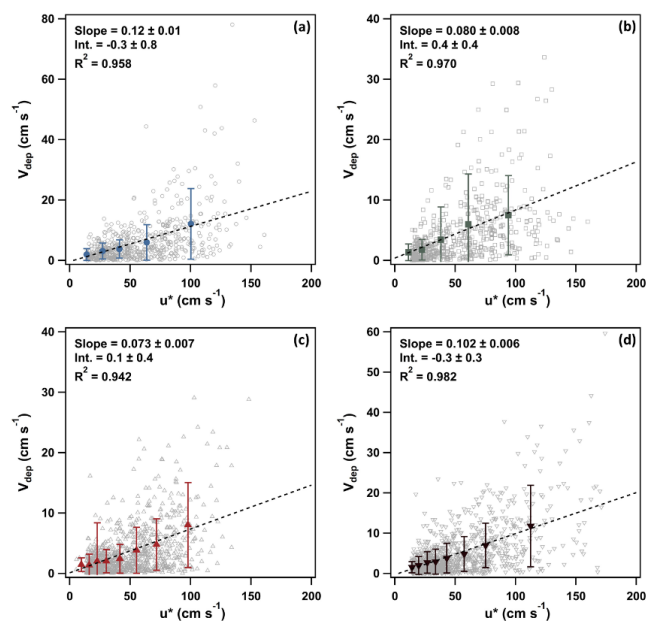
Figure 5: Total deposition velocity verses friction velocity ($u*$) for the (a) winter, (b) spring, (c) summer, and (d) fall. Grey points are raw data, and the colored markers are mean deposition binned by $u*$ (each one representing 200 measurement points), with the error bars representing standard deviation.
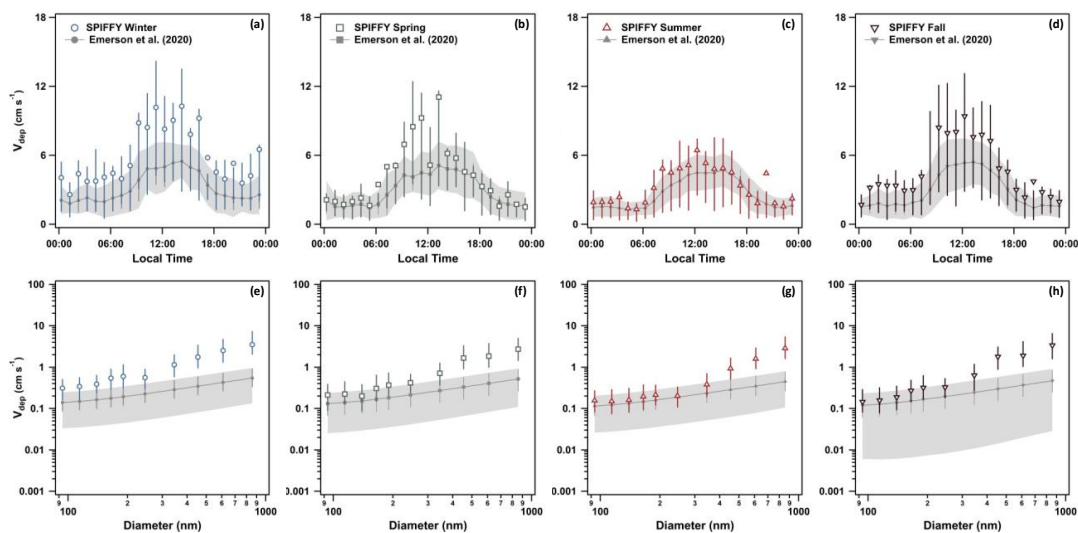
Figure 6: Average measured diel deposition velocity compared to the modeled diel deposition for the (a) winter, (b) spring, (c) summer, and (d) fall using the resistance model from Emerson et al. (2020). Additionally, seasonal size-dependent deposition trends compared to the model are shown for all seasons in panels (e) through (h). For all plots the modeled deposition is shown as closed grey markers, with shading representing the standard deviation and grey bars representing the interquartile range. Measured average data are represented as open markers with bars representing the interquartile range.

3.3 Influence of scalar gradients on seasonal deposition velocities

Phoretic effects, which are the drift of particles induced by gradients in scalars such as temperature, water vapor, and electricity, can impact particle movement. The influence of these gradients has been well studied in indoor environments (Salthammer et al., 2011), however, their contribution in outdoor forested environments is still uncertain (Farmer et al., 2021; Petroff et al., 2008). Previous studies have hypothesized that such gradients could impact particle deposition over snow and ice surfaces and impact forested environments during the winter. In their deposition model, Petroff and Zhang (2010) used a constant parameter to describe bulk phoretic effects over ice, snow, and water surfaces; this single phoretic parameter helped resolve differences between measured and modeled deposition velocities. Mammarella et al. (2011) used their measurements of particles in the Brownian diffusion dominated regime ($0.020 – 0.065$ µm) to investigate the power law dependency between normalized deposition velocity ($V_{dep}/u*$) and the Schmidt number (Sc) and found that this relationship differed for winter versus other seasons. While Mammarella et al. (2011) ultimately concluded that the strong winter deposition velocities must be due seasonal differences in size distribution, they noted that additional factors, such as electrostatic and thermophoretic forces, could contribute to the enhancement of deposition of very small particles. Here, we hypothesized that snow covered canopies during SPiFFY were affected by phoretic effects – in particular, gradients in temperature (Section 3.3.2) or turbulence (Section 3.3.2). We do not consider electrophoresis, as the findings of Tammet el al. (2001) indicate that these gradients only affect $0.01 – 0.2$ µm particles above the canopy during low-wind conditions.

3.3.1 Thermophoretic effects on deposition

We first investigated thermophoresis, which is the drift of particles caused by temperature gradients between the air and collecting surfaces, as a possible driver of the increased winter deposition caused by the low temperatures and the addition of snow to the canopy (Batchelor and Shen, 1985). We modeled these gradients using measured meteorological parameters along with a simple leaf level energy balance (**Appendix B**). This energy balance showed that in the winter, needles were consistently colder than the surrounding air during the day, while temperatures at night were comparable. Specifically, the leaf level energy balance predicted an average gradient of 4 $\pm$ 2 K between the leaf and surrounding air. Incorporating the thermophoretic settling velocity with this gradient into the Emerson et al. (2020) deposition model yielded negligible changes in the predicted particle deposition velocity. In the sub-micron size range of interest here, thermophoresis is not strongly correlated to particle size. Unrealistic gradients ($15 – 60$ K/mm) would be needed for thermophoresis to drive the observed change in size-dependent deposition. Thus, thermophoresis cannot compete with the other drivers of deposition in a needleleaf forest.

3.3.2 Movement of particles by turbophoresis

Discrepancies between models and field observations of particle deposition are common, and often attributed to missing deposition mechanisms (Saylor et al., 2019; Pryor et al., 2008). Movement of particles from areas of high to low turbulence, or turbophoresis, has been proposed as an important mechanism for dry deposition of particles in the accumulation mode (Mammarella et al., 2011; Katul and Poggi, 2010; Katul et al., 2010; Feng, 2008). Two studies successfully integrated a turbophoresis term into a size-resolved dry deposition parameterization. First, Feng (2008) developed a zero-dimensional representation of particle deposition based on the deposition in pipes. In that model, turbophoresis – referred to as the "burst effect of atmospheric eddy turbulence" – is parameterized according to the roughness Reynolds number. Later, Katul et al. (2010) developed a multi-layer model for particle dry deposition. In the Katul model, turbophoresis was parameterized according to the vertical momentum flux, or turbulent stress, and the standard deviation of the vertical velocity. Katul et al. (2010) concluded that the effects of turbophoresis were most prominent for particles between 0.1 and 10 µm above and in the upper layers of the canopy, and that the effects could be neglected for particles < 0.01 µm.

To investigate the effect of turbophoresis on the SPiFFY observations, we used the Katul et al. (2010) parameterization (**Appendix A**) because it maintains the minimum in size-dependent deposition velocity, in contrast to the Feng (2008) model. This minimum is a key characteristic of particle deposition that has emerged in recent syntheses of observations (Farmer et al., 2021; Saylor et al., 2019; Hicks et al., 2016). However, the Katul

450　parameterization has two components that may result in underestimation of deposition to the canopy. First, the model neglects interception, which has a significant role in deposition over forests. Second, the model relies on the inertial impaction term from Slinn and Slinn (1980), which was formulated for water and smooth surfaces. Katul et al. (2010) acknowledged these as possible reasons for underestimation of particle deposition and recognized the need to further consider "microroughness" of leaves and needles.

455　Single point calculations of turbophoretic velocity (V_t), following those of Katul et al. (2010), allow us to bound the possible contribution to total deposition. Turbophoretic velocity (V_t) for a 0.1 µm particle ($\tau_p = 1.4 \times 10^{-7}$ at 298 K) should be ~0.04 cm s^{-1} assuming a u* = 1.0 m s^{-1} and a leaf level boundary layer thickness of 0.15 mm. This is an order of magnitude lower than our measured deposition velocities for this size range and is therefore expected to be negligible. Using the same assumptions but for a 1 µm particle ($\tau_p = 5.0 \times 10^{-6}$ at 298 K) we estimate that V_t is ~1.3
460　cm s^{-1}, potentially resulting in a ~40% increase in the total modeled deposition for particles in that size range. This single point calculation based on the Katul parameterization indicates that turbophoresis may play a role in deposition of larger particles (≥ 1 µm). However, turbophoresis is unlikely to fully explain the seasonal differences observed during SPiFFY as the largest seasonal discrepancies occurred at the lower end of our size range.

　　To investigate the impact of turbophoresis over the entire size range and over time while accounting for challenges
465　with the Katul et al. (2010) model, we isolated the turbophoretic collection efficiency from the model and integrated it into the Emerson et al. (2020) parameterization of surface resistance (**Section 2.4.1**). We present both the resulting deposition velocities (V_{dep}) and surface resistances (R_s) – presented as velocities – from the model with ($V_{dep} + E_{turbo}$, $R_s + E_{turbo}$) and without (V_{dep}, R_s) turbophoresis in **Figure 7a**. As a sensitivity test, we varied the thickness of the viscous sublayer (b) between 5 and 50 mm following Katul et al. (2010). Turbophoresis resulted in
470　large changes for deposition of 1 – 10 µm particles, with larger changes for a thinner viscous sublayer, i.e. when $b = 5$ (**Figure 7a, 7b**). The incorporation of turbophoresis resolved some of the initial model-measurement disagreement shown in in Figure 6 for larger particles but had little effect on the model-measurement disagreement at the lower end of the measured size range. Even with the addition of turbophoresis, total deposition in the wintertime was still underpredicted by ~40% (**Figure 7c, Figure S13**). Interestingly, inclusion of the turbophoresis term also created a
475　plateau in deposition for particles greater than 10 µm (**Figure 8**). This modeled plateau is consistent with a feature frequently noted in size-resolved deposition velocity observations, particularly over needleleaf forests. Saylor et al. (2019) developed an empirical logistic equation to resolve this feature but attributed it to an unknown mechanism. Turbophoresis thus provides a potential mechanism to explain this observed feature in 1 – 10 µm size range. A more critical exploration of the turbophoresis parameterization would be needed to resolve this.

480　Both the Emerson et al. (2020) model and the integrated Emerson et al. (2020) with E_{turbo} were compared against literature values for size resolved deposition in forests (Zhang et al., 2014; Lavi et al., 2013; Gordon et al., 2011; Mammarella et al., 2011; Vong et al., 2010; Grönholm et al., 2009b; Pryor et al., 2007, 2009; GröNholm et al., 2007; Pryor, 2006; Gaman et al., 2004; Gallagher et al., 1997; Lorenz and Murphy, 1989; Waraghai and Gravenhorst, 1989; Grosch and Schmitt, 1988; Höfken and Gravenhorst, 1982). The two parameterizations were
485　both comparable to the synthesized literature data, which can be observed in **Figure 8**. For these comparisons the models were run for both a needleleaf and broadleaf condition in the midsummer, assuming $u* = 0.5$ m s^{-1}, $T = 20$ °C, and an average wind speed of 3 m s^{-1}.
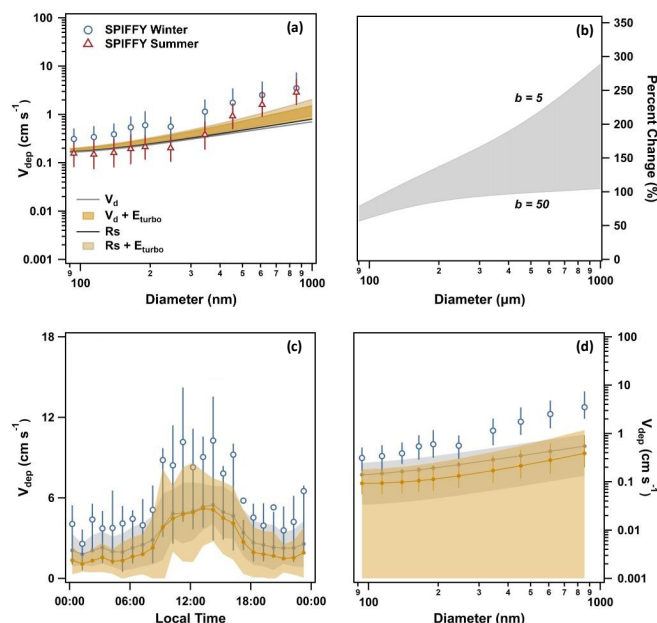
Figure 7: (a) Size resolved deposition measured during the winter (blue circles) and summer (red triangle) periods of SPiFFY compared to modeled deposition velocities from Emerson et al. (2020) (V_d; light grey line) versus Emerson et al. (2020) with the inclusion of turbophoresis collection efficiency in the surface resistance term ($V_d + E_{turbo}$; gold shaded region). Surface resistance without turbophoresis (R_s; dark grey line) and with turbophoresis incorporated ($R_s + E_{turbo}$; dark gold shaded region) are shown as velocities. The shaded range shows how the second model formulation changes with the thickness of the viscous sublayer (b); higher deposition values occur at smaller b values. (b) The percent increase in predicted deposition with the addition of turbophoresis is shown as a function of particle size. (c) The average observed (blue circles) versus predicted (shaded range) diel cycle and (d) size-dependent prediction of the model with (grey circles, grey shading) and without (gold circles, gold shading) turbophoresis considered is shown for the winter. The shading represents standard deviation; bars on data points represent the interquartile range.
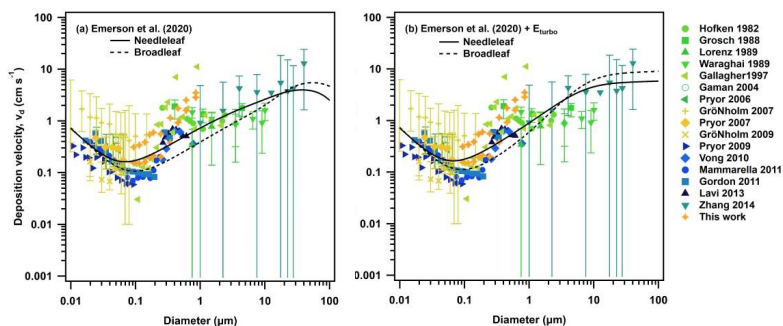
Figure 8: Comparison of (a) the Emerson et al. (2020) model alone and (b) the Emerson et al. (2020) model with the turbophoresis collection efficiency (E_{turbo}) from Katul et al. (2010) integrated into the surface resistance (R_s) term.

3.4 Influence of snow cover on deposition velocity

505

Thermophoresis and turbophoresis are not the only hypotheses proposed in the literature to explain seasonal variation in particle deposition velocities. Gallagher et al. (1992) observed a significant decrease in $3 - 31$ µm cloud droplet deposition over a snow-covered Sitka spruce canopy. That study used an isolated snow event to observe the effect of snow on deposition and found deposition was two times lower during snow cover. This snow-driven

510   suppression in V_{dep} was attributed to a decrease in surface roughness of the canopy and the subsequent increase of the effective target diameter. Changes in surface roughness from snowfall are not directly accounted for in either the Emerson et al. (2020) or the Zhang et al. (2001) model, and could contribute to model-measurement disagreement. In both model parameterizations, roughness length is used to describe surface roughness and is defined with a seasonally variable term. For an evergreen needleleaf forest, the roughness length ranges from $0.8 - 0.9$ m, with a

515   drop in the term during the midsummer and transitional spring, but not during the winter period. This approach is consistent with our measured roughness length, which did not vary substantially between seasons. During the spring SPiFFY campaign, we captured an isolated snow period, allowing us to contrast snow-covered fluxes versus prior bare forest surfaces. We observe no significant differences in the total or size-dependent deposition trends during these two periods (**Figure 9**), indicating that another mechanism, independent of snow, is driving the increased

520   wintertime deposition velocities.
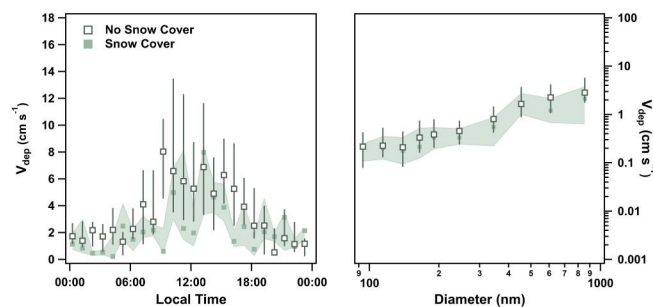
Figure 9: Average diel cycle of total deposition velocity (left) and average size-dependent deposition velocity (right) during periods of snow cover (solid green markers with shaded interquartile range) versus no snow cover (open markers with bars representing the interquartile range) from the spring.

525   ### 3.5 The role of interception and changes in the needle surface during the winter

While many deposition studies have proposed alternate mechanisms to explain the numerous model-measurement discrepancies, few have suggested tuning currently considered mechanisms by season. Below we explore aspects of dry deposition mechanisms that could be seasonally dependent. We investigate the extent to which seasonality in

530   certain deposition mechanisms and their associated parameterizations could explain the enhanced wintertime deposition velocities observed at Manitou. We do not consider roughness length (z_0) nor the characteristic radius of the collectors (A); while both terms are well established to be seasonally dependent over deciduous forests, measured roughness length did not vary strongly between seasons at SPiFFY (**Figure S2**) and the characteristic radius for an evergreen needleleaf forest is not expected to change seasonally. We first consider potential seasonality

535   in Brownian diffusion, and then interception.

As discussed above, Mammarella et al. (2011) indicated that deposition of smaller particles ($0.020 - 0.065$ µm) behaved differently in winter than in other seasons. Because the deposition of these particles is dominated by Brownian diffusion, the group investigated potential seasonality in that term. Following previous work, Mammarella et al. parameterized the Brownian collection efficiency as:

540    $$E_b = C_b Sc^{-\gamma} \tag{16}$$

where C_b and γ are constants. Proposed values for γ have historically been land use dependent but not seasonally dependent. For example, Slinn and Slinn (1980) recommend a $\gamma = 1/2$ for water surfaces and Slinn (1982) proposed that $\gamma = 2/3$ for vegetated surfaces. In the Zhang et al. (2001) and subsequent Emerson et al. (2020) model, γ is also defined as a land use dependent constant ranging from 1/2 to 2/3. Mammarella et al. (2011) found that scaling

545   observed deposition velocities with the Schmidt number (Sc) implied a much lower exponential term of $\gamma = 0.36$ in the winter, in contrast to $\gamma = 0.66$ in other seasons. While the study theorized that this was due to phoretic effects, our analyses above shows that thermo-, electro-, and turbophoretic effects are unlikely to influence particle deposition in this ultrafine size range (< 0.1 µm) under reasonable wintertime conditions in a similarly structured forest. Thus, while seasonally scaling the constants in Brownian collection efficiency terms decreased model-

550   measurement discrepancy in one instance, there is no mechanistic basis for such a shift – particularly one that only impacts Brownian diffusion related mechanisms. We note that the Schmidt number is the ratio of kinematic viscosity to diffusion coefficients, which do depend on temperature and therefore will change seasonally. However, while the Schmidt number changes by $40 \pm 7\%$ from the coldest to warmest conditions at Manitou this only results in an average change of $2 \pm 2\%$ in the deposition velocities for our measured size range (**Figure S14**). Further, as

555   our measured particle size range during SPiFFY was larger ($0.08 – 1.0$ um) than the Mammarella study, merely changing the seasonality of the Brownian diffusion term did not fully account for the observed changes in wintertime data. In fact applying this scaling to the Emerson et al. (2020) model only caused new problems in model disagreement for the SPiFFY data (**Figure S15**).

The seasonal dependence of interception is typically limited in models to considerations of roughness length and

560   collector radius – but as described above, neither vary substantially enough at Manitou to account for the enhanced wintertime deposition velocities. Plant physiological literature suggests that other aspects of needleleaf forests may undergo seasonal changes that warrant consideration in deposition. Needleleaf plants are efficient at capturing particles (Beckett et al., 1998, 2000) due to their large available surface area, thick and highly structured epicuticular wax, and high stomatal density (He et al., 2020; Räsänen et al., 2013; Sæbø et al., 2012). While surface area of

565   evergreen needleleaf trees is considered independent of season, stomatal conditions are well-established to change with environmental conditions (Räsänen et al., 2012, 2013). The seasonality and link to particle uptake of the epicuticular wax properties of evergreen needleleaf trees is less well understood, however seasonal changes in needleleaf wax structure have been observed (Altieri et al., 1994) and it has been shown that elevated temperatures can lead to smother wax structures on needles (Apple et al., 2000) Additionally, the wax can be altered and damaged

570   by uptake of pollutants which has been linked to changes in the plant's particle uptake capacity (Burkhardt and Pariyar, 2014). Studies of particle loadings collected on evergreen needleleaf trees provide some evidence of seasonality in particle collection efficiency (He et al., 2020; Zha et al., 2018; Zhang et al., 2017; Freer-Smith et al., 2005), but many of these studies lack clear linkages to leaf properties or adequate air concentration data to discern enhanced wintertime deposition velocities, rather than just deposition flux. However, changes in stomatal

575   conditions, epicuticular wax properties, and needle anatomy could be changing the flow of particles around needle surfaces and the collection efficiency of interception. Seasonal changes in plant physiology would trend with interception over other terms because interception is the only mechanism that depends strongly on particle interactions with the collecting surface. In contrast, mechanisms like Brownian motion and impaction both depend on the energy of the particle.

580   To determine whether seasonal changes in interception collection efficiency could account for enhanced wintertime deposition velocity, we used the Emerson et al. (2020) parameterization first excluding turbophoresis. Doubling the interception constant (C_{in}) from 2.5 to 5 closed the gap between the measured and modeled total and size-resolved deposition (**Figure 10, Figure S13**). This increase in the constant indicates that the collection efficiency of interception approximately doubling in the winter. Incorporating both turbophoretic processes and this seasonally

585   adjusted interception constant produces comparable model-measurement agreement as the isolated adjusted interception constant (**Figure 10, Figure S13**). However, the isolated increased interception constant produced better size-dependent agreement. The hypothesis that seasonally driven changes in plant physiology enhances particle uptake via interception mechanisms during the winter is consistent with SPiFFY data and can be accounted for with seasonally dependent interception terms.
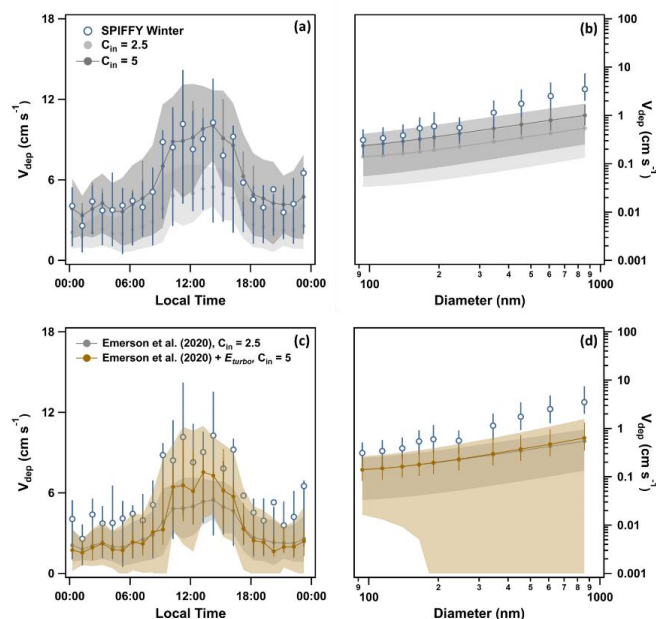
Figure 10: Average measured diel deposition velocity (a, c) and size-dependent deposition trends (b, d) compared to the original and adjusted modeled deposition for the winter. The results of the adjusted interception term are shown in (a) and (b), while the results of the adjusted interception term coupled with the inclusion of the turbophoresis term are shown in (c) and (d). For all plots the original modeled deposition is shown as closed light grey markers, with shading representing the standard deviation. The adjusted model results are shown in dark grey (a, b) and yellow (c, d) where average velocities are solid markers, shading represents the standard deviation, and bars represent the interquartile range. Measured average data are represented as open markers with bars representing the interquartile range.

4   Conclusions

Significant seasonal changes in particle trends were observed throughout the SPiFFY campaign. Particle concentration, flux, exchange velocity (V_{ex}), and deposition velocity (V_{dep}) all exhibited similar diel trends that varied in magnitude between seasons. The winter had the lowest concentrations and fluxes of particles, yet the highest deposition velocities; the summer had the highest concentrations and fluxes, with the lowest deposition velocities. The spring and fall acted as transition seasons and fell between the summer and winter trends. These differences extended to the size resolved trends in V_{dep}, with the smaller particles (0.1 – 0.3 µm) having the largest changes between seasons. The commonly-used resistance model approach for particle deposition (e.g. Emerson et al. (2020) revision of Zhang et al. (2001)) accurately described size-resolved V_{dep} and total particle V_{dep} in the summer, but was unable to predict seasonal variation or capture V_{dep} in the winter. Trends for total and size-resolved deposition velocity in the winter, spring, and fall were significantly underestimated by the model. The winter had the largest model disagreement (~90%).

The observation of enhanced deposition velocities during winter is consistent with previous particle flux data collected over forests (Mammarella et al., 2011; Rannik et al., 2009; Suni et al., 2003). The wintertime enhancement has been attributed to multiple factors, including increases in concentration of larger particles, scalar gradients (thermophoretic and turbophoretic effects) that drive particles towards surfaces, and changes in surface roughness from snow on the canopy (Mammarella et al., 2011; Rannik et al., 2009; Gallagher et al., 1992). Changes in leaf physiological properties may also enhance particle uptake. However, our quantitative understanding of the relative

impact of these factors is limited (Farmer et al., 2021; Saylor et al., 2019; Hicks et al., 2016). This data set provided the unique opportunity to probe the importance of these and other mechanisms in controlling deposition velocity
620   over an evergreen needleleaf canopy across seasons.

The particle size distribution was consistent across seasons and could not explain enhanced wintertime total particle deposition velocity. Seasonal differences in size-resolved V$_{dep}$ further indicated a missing size-dependent deposition mechanism. Using a simple leaf-level energy balance and equations outlined by Salthammer et al. (2011) and Hinds (1999), we ruled out thermophoresis as the source of enhanced V$_{dep}$. We ignored electrophoresis, which has been
625   previously shown to have a negligible influence on deposition to a canopy (Tammet et al., 2001). Using an isolated snow event during the spring measurement period, we determined snow in the canopy does not change the surface roughness enough to impact deposition mechanisms or account for the observed enhancement in wintertime deposition.

Our analyses show that both turbophoresis and interception can influence dry deposition. Incorporating the
630   turbophoresis collection efficiency term developed by Katul et al. (2010) into Emerson et al. (2020)'s surface resistance term improved model-measurement comparisons. Turbophoresis has a greater impact on larger particles (closer to 1 µm) than smaller, so is not responsible for the enhanced wintertime deposition velocity. The more interesting result from the incorporation of turbophoresis was the change in shape it created in the predicted size-dependent deposition trend for large particles (10 – 100 µm). The addition created a plateau in this size range, which
635   could help explain the shelf observed in deposition measurements over forests for particles > 10 µm. This range was outside our measured size range, but our results indicate that turbophoresis should be explored further as a mechanism for dry deposition of particles. We hypothesize that interception in the winter is also enhanced by changes in the stomatal conditions and needle structure during the winter. Needle surface structure impacts particle interactions with the surface and therefore uptake, which would be described by the interception efficiency for our
640   measured size range. We account for this factor by increasing the scaling constant for interception in the Emerson et al. (2020) model. This enhancement resolves the wintertime model-measurement discrepancy in deposition velocity and suggests further work into seasonal shifts in plant physiology of evergreen needleleaf trees is warranted. Overall, these findings support the development and addition of seasonal constants into currently used deposition modules in order to more accurately predict variation in deposition trends, particle lifetime, and the impact of
645   particles on both air quality and radiative properties.

Appendix A: Outline of Deposition Model Frameworks and Parameterizations

We used two main models to explore the roles and possible seasonal changes of deposition mechanisms. The first was a resistance model developed by Emerson et al. (2020), which is based on the models presented by Zhang et al.
650   (2001) and Slinn (1982). This model considered four main deposition mechanisms: Brownian motion, gravitational settling, interception, and impaction. Deposition velocity in the Emerson et al. (2020) model is defined using the gravitational settling velocity (V_g), the aerodynamic resistance (R_a), and the surface resistance (R_s).

$$V_d(d_p) = V_g(d_p) + \frac{1}{R_a + R_s} \tag{A1}$$

$$V_g(d_p) = \frac{d_p^2 \, \rho_p \, g \, C_c}{18 \, \eta} \tag{A2}$$

$$R_a = \frac{\ln\left(\frac{z_r}{z_0}\right) - \psi_H}{\kappa \, u^*} \tag{A3}$$

$$R_s = \frac{1}{\varepsilon_0 \, u^* \, (E_b + E_{im} + E_{in}) \, R_1} \tag{A4}$$

$$R_1 = e^{-St^{1/2}} \tag{A5}$$

$$E_b = C_b Sc^{-2/3} \tag{A6}$$

$$E_{im} = C_{im} \left(\frac{St}{\alpha + St} \right)^{\beta} \tag{A7}$$

660
$$E_{in} = C_{in} \left(\frac{d_p}{A} \right)^{\upsilon} \tag{A8}$$

In these equations d_p is the particle diameter, ρ_p is the density of the particle, g is the gravitational acceleration, C_c is the Cunningham slip correction factor, η is the kinematic viscosity of air, z_r is measurement height, z_0 is the roughness length, ψ_H is the stability function, St is the stokes number, and Sc is the Schmidt number. The set variables are $C_b = 0.2$, $C_{im} = 0.4$, $\beta = 1.7$, $C_{in} = 2.5$, and $\upsilon = 0.8$ while the variables α and A are land use dependent

665   and can be found in the original Zhang et al. (2001) publication.

The second model that we explored was from Katul et al. (2010), who presented a multi-layer model that considered the mechanisms of Brownian motion, gravitational settling, impaction, and turbophoresis. This model defined the quasi-laminar boundary layer resistance, or surface resistance, according to the equations outlined by Seinfeld and Pandis (1998) and added an additional term describing turbophoresis.

670
$$R_s = \frac{1}{\sqrt{-\overline{u'w'(z)}}\left(\theta Sc^{-2/3} + 10^{-3/St_t} + V_t\right)} \tag{A9}$$

Here $\overline{u'w'(z)}$ is the vertical momentum flux or turbulent stress, θ describes the ratio of the viscous and drag coefficient of the leaf, St_t is the turbulent Stokes number, and V_t is the turbophoretic velocity.

$$\theta = \frac{\pi}{2} \left(\frac{c_v}{c_d} \right) \tag{A10}$$

$$St_t(z) = \frac{V_g \left(-\overline{u'w'(z)} \right)}{g\,\eta} \tag{A11}$$

675
$$V_t(z) = \frac{\tau_p}{1 + \frac{\tau_p}{\tau(z)}} \left(\frac{\sigma_w^2(z)}{\pi\,b\,\eta} \right) \tag{A12}$$

$$\tau_p = \frac{d_p^2\,\rho_p\,C_c}{18\,\eta} \tag{A13}$$

$$\tau = \frac{K_t}{\sigma_w^2} \tag{A14}$$

$$K_t = \frac{-\overline{u'w'}}{\left| \frac{\delta \overline{U}}{\delta z} \right|} \tag{A15}$$

The variable notation follows those described above. The additional variables are τ_p which is the particle relaxation

680   time, τ is the Lagrangian turbulent timescale, σ_w is the standard deviation of the vertical velocity, and b which is the thickness of the viscous sublayer for the vertical velocity variance. Katul et al. (2010) used $b = 25$ m and defined an acceptable range for the value as $5 < b < 50$ m. For the calculation of the Lagrangian turbulent timescale, K_t is the eddy viscosity of the flow and is calculated using the vertical momentum flux and the mean longitudinal velocity ($\overline{U}$). These terms are either in relation to or integrated over the height of the canopy (z). It should be noted that for all

685   equations outlined here, some of the variable notation has been changed from the original papers in order to have consistent references in this work.

Appendix B: Equations and Results for Leaf Level Energy Balance and Thermophoretic Settling Velocity

Both real time data and parameters derived from other literature were used to create the leaf level energy balance

690   equation used in this work. Real time measurements of photosynthetically active radiation (*PAR*), air temperature (T_{air}), wind speed (*WS*), and relative humidity (*RH*) were used (Frank et al., 2021). The PAR was converted into short-wave radiation (*SWR*) using the following conversion from Thimijan and Heins (1983):

$$SWR = \left(\frac{PAR}{4.57} \right) \tag{B1}$$

695 An average stomatal conductance of 0.08 ± 0.05 mol m^{-2} s^{-1} was derived from reported literature values (Harley et al., 2014; Calder et al., 2010; McDowell et al., 2008; Sala et al., 2005; Domec et al., 2004; Skov et al., 2004; Hubbard et al., 1999, 2001; Panek and Goldstein, 2001; Ryan et al., 2000; Zhang et al., 1997; Monson and Grant, 1989). Defined parameters and constants used in the model are listed in **Tables B1** and **B2**. The following series of equations were used to form the leaf level energy balance and predict temperature gradients between the air and collecting surface.

700 Saturation vapor pressure (kPa):

$$e_{sat} = a \, e^{\frac{b \, T_{air}}{(T_{air}+z)}} \tag{B2}$$

Water Vapor Pressure of the air (kPa):

$$e_a = e_{sat} \left(\frac{RH}{100}\right) \tag{B3}$$

Slope of the e$_{sat}$/T curve (kPa °C^{-1}):

705 $$s = \frac{e_{sat} \, b \, c}{(T_{air}+z)^2} \tag{B4}$$

Water vapor pressure deficit of the air (kPa):

$$VPD = e_{sat} - e_a \tag{B5}$$

Absorbed short-wave radiation (W m^{-2}):

$$SWR_{abs} = a_{SWR} \cos(i) \, SWR \tag{B6}$$

710 Incoming long-wave radiation (W m^{-2}):

$$LWR_{in} = 1.31 \left(\frac{10 \, e_a}{T_{air}}\right)^{1/7} \sigma_{SB} (T_{air} + 273.15)^4 \tag{B7}$$

Isothermal outgoing long-wave radiation (W m^{-2}):

$$LWR_{out,i} = \varepsilon \, \sigma_{SB} (T_{air} + 273.15)^4 \tag{B8}$$

Isothermal net radiation (W m^{-2}):

715 $$R_{ni} = SWR_{abs} + LWR_{in} - LWR_{out,i} \tag{B9}$$

Leaf boundary-layer resistance (s m^{-1}):

$$r_{bl} = \frac{1}{\left(1.5 \, g_x \frac{(WS)^{Jx}}{d^{1-Jx}}\right)} \tag{B10}$$

Radiative resistance (s m^{-1}):

$$r_r = \frac{\rho_{air} \, c_p}{4 \, \varepsilon \, \sigma_{SB} (T_{air}+273.15)^3} \tag{B11}$$

720 Boundary-layer & radiative resistance (s m^{-1}):

$$r_{blr} = \frac{1}{\left(r_{bl}^{-1} + r_r^{-1}\right)} \tag{B12}$$

Modified psychrometric constant (kPa K^{-1}):

$$y_m = y \left(\frac{r_{st}}{r_{blr}}\right) \tag{B13}$$

Atmospheric
Chemistry
and Physics
Open Access
Discussions
EGU

Leaf-to-air temperature difference (C):

725 $$\Delta T = \left(\frac{y_m\, R_{ni}\, r_{blr}}{\rho_{air}\, C_p - VPD} \right) \frac{1}{(s + y_m)} \tag{B14}$$

Leaf temperature (C):

$$T_{leaf} = T_{air} + \Delta T \tag{B15}$$

The resulting diel modeled gradients for the winter measurement period are shown in **Figure B1**.

Table B1: Leaf level parameters defined for the energy balance.

| Parameter	Units	Value
Angle from horizontal (i)	degrees	$0 - 90$
Absorptance to SWR (a_{SWR})	%	$0.4 - 0.6$
Emissivity (ε)	none	$0.96 - 0.98$
Characteristic dimension (d)	mm	1 *
Shape factor of the leaf (shape)	none	2 **
Stomatal resistance (r_{st})	s m^{-1}	11.76***

*Defined for a pine needle
**Shape = 2 indicates a cylindrical shape
***Value obtained through synthesis of various reported values in the literature for
ponderosa pines under normal, unstressed conditions.

730

Table B2: Constants used in the formulation of the leaf level energy balance, defined in the order in which they appear in Table S3.

Constant	Units	Value
Coefficient in e_{sat} equation (a)	kPa	0.61121
Coefficient in e_{sat} equation (b)	none	17.502
Coefficient in e_{sat} equation (z)	°C	240.97
Stefan-Boltzman constant (σ_{SB})	W m^{-2} K^{-4}	5.67 x 10^{-8}
Coefficient in r_{bl} equation for a flat leaf shape (g_{flat})	m	0.00662
Coefficient in r_{bl} equation for a cylinder leaf shape (g_{cyl})	m	0.00403
Coefficient in r_{bl} equation for a sphere leaf shape (g_{sph})	m	0.00571
Coefficient in r_{bl} equation for a flat leaf shape (j_{flat})	none	0.5
Coefficient in r_{bl} equation for a cylinder leaf shape (j_{cyl})	none	0.6
Coefficient in r_{bl} equation for a sphere leaf shape (j_{sph})	none	0.6
Density of air (ρ_{air})	kg m^{-3}	1.292
Heat capacity of air (C_p)	J kg^{-1} K^{-1}	1010
Psychrometric constant (y)	kPa K^{-1}	0.066
Latent heat of vaporization (L)	J g^{-1}	2500
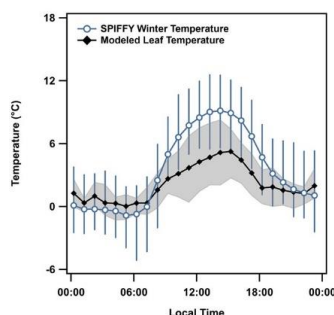
Figure B1: Diel average measured air temperature and modeled leaf temperature. With the interquartile range for the measured data shown in bars and the interquartile range for the modeled data shown in shading.

Thermophoretic settling velocity was calculated according to the following equations outlined by Salthammer et al. (2011) and Hinds (1999). The velocity was calculated as:

$$V_{TH} = \frac{3 \, v \, C_c \, H \, \Delta T}{2 \, \rho_{air} \, T_{air}}$$ (B16)

using the viscosity of air (v), Cunningham slip correction (C_c), temperature gradient between the collecting surface and air (ΔT), density of air (ρ_{air}), and temperature of air (T_{air}). The H term was separately calculated by:

$$H = \frac{1}{1+6\left(\frac{\lambda}{D_a}\right)} \times \frac{\left(\frac{k_a}{k_p}\right)+4.4\left(\frac{\lambda}{D_a}\right)}{1+2\left(\frac{k_a}{k_p}\right)+8.8\left(\frac{\lambda}{D_a}\right)}$$ (B17)

using the mean free path (λ), aerodynamic diameter of the particle (D_a), the thermal conductivity of air (k_a), and the thermal conductivity of the particles (k_p). The behavior of the thermophoretic settling velocity as the magnitude of the temperature gradient changes and the thermal conductivity of the particles change is shown in **Figure B2**, along with the results of its integration into the Emerson et al. (2020) model.
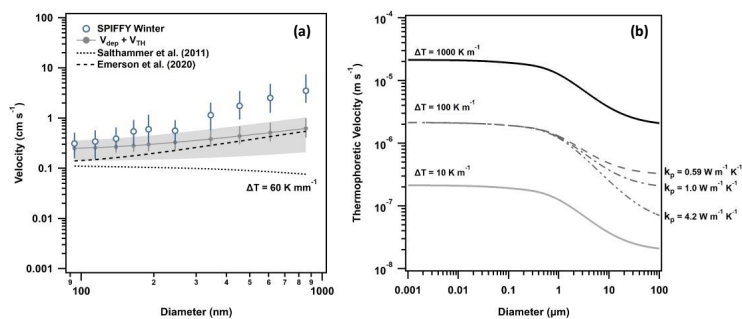
Figure B2: (**a**) Integration of the thermophoretic velocity into the Emerson et al. (2020) model. The total modeled velocity is shown in grey with shading representing the standard deviation and bars representing the interquartile range. (**b**) Thermophoretic settling velocity as a function of particle diameter for three different gradient values: ΔT = 10, 100, and 1000 K m^{-1}. Additionally, the velocity at ΔT = 100 K m^{-1} was varied by particle thermal conductivity and results are shown for k_p = 0.59, 1.0, and 4.2 W m^{-1} K^{-1}.

Data availability

Data is available at https://manitou.acom.ucar.edu/ with other data from the campaign.

755   *Author contribution*

EKB preformed the analysis presented in this work and prepared the manuscript with contributions from all co-authors. HMD and RF collected the measurements during the SPiFFY campaign in 2016 and provided critical insight into the finer details of the dataset. EWE developed the code used analyze the data. DFK planned the campaign and guided the research. All authors reviewed and edited the manuscript.

References

Ahlm, L., Krejci, R., Nilsson, E. D., Mårtensson, E. M., Vogt, M., and Artaxo, P.: Emission and dry deposition of accumulation mode particles in the Amazon Basin, 10, 10237–10253, https://doi.org/10.5194/acp-10-10237-2010, 770   2010.

Altieri, A., Del Caldo, L., and Manes, F.: Morphology of epicuticular waxes in Pinus pinea needles in relation to season and pollution-climate, 24, 79–91, https://doi.org/10.1111/j.1439-0329.1994.tb01061.x, 1994.

Apple, M. E., Olszyk, D. M., Ormrod, D. P., Lewis, J., Southworth, D., and Tingey, D. T.: Morphology and Stomatal Function of Douglas Fir Needles Exposed to Climate Change: Elevated CO2 and Temperature, 161, 127–775   132, https://doi.org/10.1086/314237, 2000.

Batchelor, G. K. and Shen, C.: Thermophoretic deposition of particles in gas flowing over cold surfaces, 107, 21–37, https://doi.org/10.1016/0021-9797(85)90145-6, 1985.

Beckett, K. P., Freer-Smith, P. H., and Taylor, G.: Urban woodlands: their role in reducing the effects of particulate pollution, Environmental Pollution, 99, 347–360, https://doi.org/10.1016/S0269-7491(98)00016-5, 1998.

780   Beckett, K. P., Freer-Smith, P. H., and Taylor, G.: Particulate pollution capture by urban trees: effect of species and windspeed, 6, 995–1003, https://doi.org/10.1046/j.1365-2486.2000.00376.x, 2000.

Billesbach, D. P.: Estimating uncertainties in individual eddy covariance flux measurements: A comparison of methods and a proposed new method, Agricultural and Forest Meteorology, 151, 394–405, https://doi.org/10.1016/j.agrformet.2010.12.001, 2011.

785   Burkhardt, J. and Pariyar, S.: Particulate pollutants are capable to 'degrade' epicuticular waxes and to decrease the drought tolerance of Scots pine (Pinus sylvestris L.), Environmental Pollution, 184, 659–667, https://doi.org/10.1016/j.envpol.2013.04.041, 2014.

Cai, Y., Montague, D. C., Mooiweer-Bryan, W., and Deshler, T.: Performance characteristics of the ultra high sensitivity aerosol spectrometer for particles between 55 and 800nm: Laboratory and field studies, Journal of 790   Aerosol Science, 39, 759–769, https://doi.org/10.1016/j.jaerosci.2008.04.007, 2008.

Calder, W. J., Lifferth, G., Moritz, M. A., and Clair, S. B. S.: Physiological Effects of Smoke Exposure on Deciduous and Conifer Tree Species, 2010, e438930, https://doi.org/10.1155/2010/438930, 2010.

Carslaw, K. S., Lee, L. A., Reddington, C. L., Pringle, K. J., Rap, A., Forster, P. M., Mann, G. W., Spracklen, D. V.,
Woodhouse, M. T., Regayre, L. A., and Pierce, J. R.: Large contribution of natural aerosols to uncertainty in indirect
795 forcing, 503, 67–71, https://doi.org/10.1038/nature12674, 2013.

Casquero-Vera, J. A., Lyamani, H., Titos, G., Moreira, G. de A., Benavent-Oltra, J. A., Conte, M., Contini, D., Järvi,
L., Olmo-Reyes, F. J., and Alados-Arboledas, L.: Aerosol number fluxes and concentrations over a southern
European urban area, Atmospheric Environment, 269, 118849, https://doi.org/10.1016/j.atmosenv.2021.118849,
2022.

800 Deventer, M. J., Held, A., El-Madany, T. S., and Klemm, O.: Size-resolved eddy covariance fluxes of nucleation to
accumulation mode aerosol particles over a coniferous forest, Agricultural and Forest Meteorology, 214–215, 328–
340, https://doi.org/10.1016/j.agrformet.2015.08.261, 2015.

Domec, J.-C., Warren, J. M., Meinzer, F. C., Brooks, J. R., and Coulombe, R.: Native root xylem embolism and
stomatal closure in stands of Douglas-fir and ponderosa pine: mitigation by hydraulic redistribution, Oecologia, 141,
805 7–16, https://doi.org/10.1007/s00442-004-1621-4, 2004.

Emerson, E. W., Hodshire, A. L., DeBolt, H. M., Bilsback, K. R., Pierce, J. R., McMeeking, G. R., and Farmer, D.
K.: Revisiting particle dry deposition and its role in radiative effect estimates, PNAS,
https://doi.org/10.1073/pnas.2014761117, 2020.

Fairall, C. W.: Interpretation of eddy-correlation measurements of particulate deposition and aerosol flux,
810 Atmospheric Environment (1967), 18, 1329–1337, https://doi.org/10.1016/0004-6981(84)90041-6, 1984.

Farmer, D. K., Boedicker, E. K., and DeBolt, H. M.: Dry Deposition of Atmospheric Aerosols: Approaches,
Observations, and Mechanisms, Annu. Rev. Phys. Chem., https://doi.org/10.1146/annurev-physchem-090519-
034936, 2021.

Feng, J.: A size-resolved model and a four-mode parameterization of dry deposition of atmospheric aerosols, 113,
815 https://doi.org/10.1029/2007JD009004, 2008.

Finkelstein, P. L. and Sims, P. F.: Sampling error in eddy correlation flux measurements, 106, 3503–3509,
https://doi.org/10.1029/2000JD900731, 2001.

Finnigan, J.: Turbulence in Plant Canopies, Annu. Rev. Fluid Mech., 32, 519–571,
https://doi.org/10.1146/annurev.fluid.32.1.519, 2000.

820 Foken, Th. and Wichura, B.: Tools for quality assessment of surface-based flux measurements, Agricultural and
Forest Meteorology, 78, 83–105, https://doi.org/10.1016/0168-1923(95)02248-1, 1996.

Frank, J. M., Fornwalt, P. J., Asherin, L. A., and Alton, S. K.: Manitou Experimental Forest hourly meteorology
data, 3rd ed., Forest Service Research Data Archive, Fort Collins, CO, 2021.

Freer-Smith, P. H., Beckett, K. P., and Taylor, G.: Deposition velocities to Sorbus aria, Acer campestre, Populus
825 deltoides × trichocarpa 'Beaupré', Pinus nigra and × Cupressocyparis leylandii for coarse, fine and ultra-fine
particles in the urban environment, Environmental Pollution, 133, 157–167,
https://doi.org/10.1016/j.envpol.2004.03.031, 2005.

Fulgham, S. R., Brophy, P., Link, M., Ortega, J., Pollack, I., and Farmer, D. K.: Seasonal Flux Measurements over a
Colorado Pine Forest Demonstrate a Persistent Source of Organic Acids, ACS Earth Space Chem., 3, 2017–2032,
830 https://doi.org/10.1021/acsearthspacechem.9b00182, 2019.

Gallagher, M. W., Beswick, K. M., and Choularton, T. W.: Measurement and modelling of cloudwater deposition to
a snow-covered forest canopy, Atmospheric Environment. Part A. General Topics, 26, 2893–2903,
https://doi.org/10.1016/0960-1686(92)90281-O, 1992.

Atmospheric
Chemistry
and Physics
Discussions

835   Gallagher, M. W., Beswick, K. M., Duyzer, J., Westrate, H., Choularton, T. W., and Hummelshøj, P.: Measurements of aerosol fluxes to speulder forest using a micrometeorological technique, 31, 359–373, https://doi.org/10.1016/S1352-2310(96)00057-X, 1997.

Gaman, A., Rannik, Ü., Aalto, P., Pohja, T., Siivola, E., Kulmala, M., and Vesala, T.: Relaxed Eddy Accumulation System for Size-Resolved Aerosol Particle Flux Measurements, J. Atmos. Oceanic Technol., 21, 933–943, https://doi.org/10.1175/1520-0426(2004)021<0933:REASFS>2.0.CO;2, 2004.

840   Gordon, M., Staebler, R. M., Liggio, J., Vlasenko, A., Li, S.-M., and Hayden, K.: Aerosol flux measurements above a mixed forest at Borden, Ontario, 11, 6773–6786, https://doi.org/10.5194/acp-11-6773-2011, 2011.

GröNholm, T., Aalto, P. P., Hiltunen, V. J., Rannik, Ül., Rinne, J., Laakso, L., HyvöNen, S., Vesala, T., and Kulmala, M.: Measurements of aerosol particle dry deposition velocity using the relaxed eddy accumulation technique, 59, 381–386, https://doi.org/10.1111/j.1600-0889.2007.00268.x, 2007.

845   Grönholm, T., Launiainen, S., Ahlm, L., Mårtensson, E. M., Kulmala, M., Vesala, T., and Nilsson, E. D.: Aerosol particle dry deposition to canopy and forest floor measured by two-layer eddy covariance system, 114, https://doi.org/10.1029/2008JD010663, 2009a.

Grönholm, T., Launiainen, S., Ahlm, L., Mårtensson, E. M., Kulmala, M., Vesala, T., and Nilsson, E. D.: Aerosol particle dry deposition to canopy and forest floor measured by two-layer eddy covariance system, 114, 850   https://doi.org/10.1029/2008JD010663, 2009b.

Grosch, S. and Schmitt, G.: Experimental Investigations on the Deposition of Trace Elements in Forest Areas, in: Environmental Meteorology: Proceedings of an International Symposium held in Würzburg, F.R.G., 29 September – 1 October 1987, edited by: Grefen, K. and Löbel, J., Springer Netherlands, Dordrecht, 201–216, https://doi.org/10.1007/978-94-009-2939-5_15, 1988.

855   Harley, P., Eller, A., Guenther, A., and Monson, R. K.: Observations and models of emissions of volatile terpenoid compounds from needles of ponderosa pine trees growing in situ: control by light, temperature and stomatal conductance, Oecologia, 176, 35–55, https://doi.org/10.1007/s00442-014-3008-5, 2014.

He, C., Qiu, K., Alahmad, A., and Pott, R.: Particulate matter capturing capacity of roadside evergreen vegetation during the winter season, Urban Forestry & Urban Greening, 48, 126510, 860   https://doi.org/10.1016/j.ufug.2019.126510, 2020.

Hicks, B. B., Saylor, R. D., and Baker, B. D.: Dry deposition of particles to canopies—A look back and the road forward, 121, 14,691-14,707, https://doi.org/10.1002/2015JD024742, 2016.

Hinds, W. C.: Aerosol Technology: Properties, Behavior, and Measurement of Airborne Particles, 2nd ed., John Wiley & Sons, Inc., New York, NY, 1999.

865   Höfken, K. D. and Gravenhorst, G.: Deposition of Atmospheric Aerosol Particles to Beech- and Spruce Forest, in: Deposition of Atmospheric Pollutants: Proceedings of a Colloquium held at Oberursel/Taunus, West Germany, 9–11 November 1981, edited by: Georgii, H.-W. and Pankrath, J., Springer Netherlands, Dordrecht, 191–194, https://doi.org/10.1007/978-94-009-7864-5_19, 1982.

Hubbard, R. M., Bond, B. J., and Ryan, M. G.: Evidence that hydraulic conductance limits photosynthesis in old 870   Pinus ponderosa trees, Tree Physiol, 19, 165–172, https://doi.org/10.1093/treephys/19.3.165, 1999.

Hubbard, R. M., Ryan, M. G., Stiller, V., and Sperry, J. S.: Stomatal conductance and photosynthesis vary linearly with plant hydraulic conductance in ponderosa pine, 24, 113–121, https://doi.org/10.1046/j.1365-3040.2001.00660.x, 2001.

875 Katul, G. G. and Poggi, D.: The Influence of Hilly Terrain on Aerosol-Sized Particle Deposition into Forested
     Canopies, Boundary-Layer Meteorol, 135, 67–88, https://doi.org/10.1007/s10546-009-9459-2, 2010.

     Katul, G. G., Grönholm, T., Launiainen, S., and Vesala, T.: Predicting the dry deposition of aerosol-sized particles
     using layer-resolved canopy and pipe flow analogy models: Role of turbophoresis, 115,
     https://doi.org/10.1029/2009JD012853, 2010.

880 Langford, B., Acton, W., Ammann, C., Valach, A., and Nemitz, E.: Eddy-covariance data with low signal-to-noise
     ratio: time-lag determination, uncertainties and limit of detection, 8, 4197–4213, https://doi.org/10.5194/amt-8-
     4197-2015, 2015.

     Lavi, A., Farmer, D. K., Segre, E., Moise, T., Rotenberg, E., Jimenez, J. L., and Rudich, Y.: Fluxes of Fine Particles
     Over a Semi-Arid Pine Forest: Possible Effects of a Complex Terrain, 47, 906–915,
     https://doi.org/10.1080/02786826.2013.800940, 2013.

885 Lee, L. A., Carslaw, K. S., Pringle, K. J., and Mann, G. W.: Mapping the uncertainty in global CCN using
     emulation, 12, 9739–9751, https://doi.org/10.5194/acp-12-9739-2012, 2012.

     Lee, L. A., Pringle, K. J., Reddington, C. L., Mann, G. W., Stier, P., Spracklen, D. V., Pierce, J. R., and Carslaw, K.
     S.: The magnitude and causes of uncertainty in global model simulations of cloud condensation nuclei, 13, 8879–
     8914, https://doi.org/10.5194/acp-13-8879-2013, 2013.

890 Lorenz, R. and Murphy, C. E.: Dry deposition of particles to a pine plantation, Boundary-Layer Meteorol, 46, 355–
     366, https://doi.org/10.1007/BF00172241, 1989.

     Mammarella, I., Rannik, Ü., Aalto, P., Keronen, P., Vesala, T., and Kulmala, M.: Long-term aerosol particle flux
     observations. Part II: Particle size statistics and deposition velocities, Atmospheric Environment, 45, 3794–3805,
     https://doi.org/10.1016/j.atmosenv.2011.04.022, 2011.

895 Massman, W. J.: A simple method for estimating frequency response corrections for eddy covariance systems,
     Agricultural and Forest Meteorology, 104, 185–198, https://doi.org/10.1016/S0168-1923(00)00164-7, 2000.

     McDowell, N. G., White, S., and Pockman, W. T.: Transpiration and stomatal conductance across a steep climate
     gradient in the southern Rocky Mountains, 1, 193–204, https://doi.org/10.1002/eco.20, 2008.

     Monson, R. K. and Grant, M. C.: Experimental Studies of Ponderosa Pine. Iii. Differences in Photosynthesis,
900 Stomatal Conductance, and Water-Use Efficiency Between Two Genetic Lines, 76, 1041–1047,
     https://doi.org/10.1002/j.1537-2197.1989.tb15085.x, 1989.

     Ortega, J., Turnipseed, A., Guenther, A. B., Karl, T. G., Day, D. A., Gochis, D., Huffman, J. A., Prenni, A. J., Levin,
     E. J. T., Kreidenweis, S. M., DeMott, P. J., Tobo, Y., Patton, E. G., Hodzic, A., Cui, Y. Y., Harley, P. C.,
     Hornbrook, R. S., Apel, E. C., Monson, R. K., Eller, A. S. D., Greenberg, J. P., Barth, M. C., Campuzano-Jost, P.,
905 Palm, B. B., Jimenez, J. L., Aiken, A. C., Dubey, M. K., Geron, C., Offenberg, J., Ryan, M. G., Fornwalt, P. J.,
     Pryor, S. C., Keutsch, F. N., DiGangi, J. P., Chan, A. W. H., Goldstein, A. H., Wolfe, G. M., Kim, S., Kaser, L.,
     Schnitzhofer, R., Hansel, A., Cantrell, C. A., Mauldin, R. L., and Smith, J. N.: Overview of the Manitou
     Experimental Forest Observatory: site description and selected science results from 2008 to 2013, 14, 6345–6367,
     https://doi.org/10.5194/acp-14-6345-2014, 2014.

910 Panek, J. A. and Goldstein, A. H.: Response of stomatal conductance to drought in ponderosa pine: implications for
     carbon and ozone uptake, Tree Physiology, 21, 337–344, https://doi.org/10.1093/treephys/21.5.337, 2001.

     Papale, D., Reichstein, M., Aubinet, M., Canfora, E., Bernhofer, C., Kutsch, W., Longdoz, B., Rambal, S., Valentini,
     R., Vesala, T., and Yakir, D.: Towards a standardized processing of Net Ecosystem Exchange measured with eddy
     covariance technique: algorithms and uncertainty estimation, 3, 571–583, https://doi.org/10.5194/bg-3-571-2006,
915 2006.

Petroff, A. and Zhang, L.: Development and validation of a size-resolved particle dry deposition scheme for application in aerosol transport models, 3, 753–769, https://doi.org/10.5194/gmd-3-753-2010, 2010.

Petroff, A., Mailliat, A., Amielh, M., and Anselmet, F.: Aerosol dry deposition on vegetative canopies. Part I: Review of present knowledge, Atmospheric Environment, 42, 3625–3653,
920   https://doi.org/10.1016/j.atmosenv.2007.09.043, 2008.

Petroff, A., Murphy, J. G., Thomas, S. C., and Geddes, J. A.: Size-resolved aerosol fluxes above a temperate broadleaf forest, Atmospheric Environment, 190, 359–375, https://doi.org/10.1016/j.atmosenv.2018.07.012, 2018.

Poggi, D., Porporato, A., Ridolfi, L., Albertson, J. D., and Katul, G. G.: The Effect of Vegetation Density on Canopy Sub-Layer Turbulence, Boundary-Layer Meteorology, 111, 565–587,
925   https://doi.org/10.1023/B:BOUN.0000016576.05621.73, 2004.

Pryor, S. C.: Size-resolved particle deposition velocities of sub-100nm diameter particles over a forest, Atmospheric Environment, 40, 6192–6200, https://doi.org/10.1016/j.atmosenv.2006.04.066, 2006.

Pryor, S. C., Larsen, S. E., Sørensen, L. L., Barthelmie, R. J., Grönholm, T., Kulmala, M., Launiainen, S., Rannik, Ü., and Vesala, T.: Particle fluxes over forests: Analyses of flux methods and functional dependencies, 112,
930   https://doi.org/10.1029/2006JD008066, 2007.

Pryor, S. C., Gallagher, M., Sievering, H., Larsen, S. E., Barthelmie, R. J., Birsan, F., Nemitz, E., Rinne, J., Kulmala, M., Grönholm, T., Taipale, R., and Vesala, T.: A review of measurement and modelling results of particle atmosphere–surface exchange, 60, 42–75, https://doi.org/10.1111/j.1600-0889.2007.00298.x, 2008.

Pryor, S. C., Barthelmie, R. J., Spaulding, A. M., Larsen, S. E., and Petroff, A.: Size-resolved fluxes of sub-100-nm
935   particles over forests, 114, https://doi.org/10.1029/2009JD012248, 2009.

Pryor, S. C., Barthelmie, R. J., and Hornsby, K. E.: Size-Resolved Particle Fluxes and Vertical Gradients over and in a Sparse Pine Forest, 47, 1248–1257, https://doi.org/10.1080/02786826.2013.831974, 2013.

Pryor, S. C., Barthelmie, R. J., Larsen, S. E., and Sørensen, L. L.: Ultrafine particle number fluxes over and in a deciduous forest, 122, 405–422, https://doi.org/10.1002/2016JD025854, 2017.

940   Rannik, Ü., Mammarella, I., Aalto, P., Keronen, P., Vesala, T., and Kulmala, M.: Long-term aerosol particle flux observations part I: Uncertainties and time-average statistics, Atmospheric Environment, 43, 3431–3439, https://doi.org/10.1016/j.atmosenv.2009.02.049, 2009.

Räsänen, J. V., Yli-Pirilä, P., Holopainen, T., Joutsensaari, J., Pasanen, P., and Kivimäenpää, M.: Soil drought increases atmospheric fine particle capture efficiency of Norway spruce, Boreal Env. Res., 17, 21–30, 2012.

945   Räsänen, J. V., Holopainen, T., Joutsensaari, J., Ndam, C., Pasanen, P., Rinnan, Å., and Kivimäenpää, M.: Effects of species-specific leaf characteristics and reduced water availability on fine particle capture efficiency of trees, Environmental Pollution, 183, 64–70, https://doi.org/10.1016/j.envpol.2013.05.015, 2013.

Reichstein, M., Falge, E., Baldocchi, D., Papale, D., Aubinet, M., Berbigier, P., Bernhofer, C., Buchmann, N., Gilmanov, T., Granier, A., Grünwald, T., Havránková, K., Ilvesniemi, H., Janous, D., Knohl, A., Laurila, T., Lohila,
950   A., Loustau, D., Matteucci, G., Meyers, T., Miglietta, F., Ourcival, J.-M., Pumpanen, J., Rambal, S., Rotenberg, E., Sanz, M., Tenhunen, J., Seufert, G., Vaccari, F., Vesala, T., Yakir, D., and Valentini, R.: On the separation of net ecosystem exchange into assimilation and ecosystem respiration: review and improved algorithm, 11, 1424–1439, https://doi.org/10.1111/j.1365-2486.2005.001002.x, 2005.

Ryan, M. G., Bond, B. J., Law, B. E., Hubbard, R. M., Woodruff, D., Cienciala, E., and Kucera, J.: Transpiration
955   and whole-tree conductance in ponderosa pine trees of different heights, Oecologia, 124, 553–560, https://doi.org/10.1007/s004420000403, 2000.

Sæbø, A., Popek, R., Nawrot, B., Hanslin, H. M., Gawronska, H., and Gawronski, S. W.: Plant species differences in particulate matter accumulation on leaf surfaces, Science of The Total Environment, 427–428, 347–354, https://doi.org/10.1016/j.scitotenv.2012.03.084, 2012.

960 Sala, A., Peters, G. D., McIntyre, L. R., and Harrington, M. G.: Physiological responses of ponderosa pine in western Montana to thinning, prescribed fire and burning season, Tree Physiology, 25, 339–348, https://doi.org/10.1093/treephys/25.3.339, 2005.

Salthammer, T., Fauck, C., Schripp, T., Meinlschmidt, P., Willenborg, S., and Moriske, H.-J.: Effect of particle concentration and semi-volatile organic compounds on the phenomenon of 'black magic dust' in dwellings, Building 965 and Environment, 46, 1880–1890, https://doi.org/10.1016/j.buildenv.2011.03.008, 2011.

Saylor, R. D., Baker, B. D., Lee, P., Tong, D., Pan, L., and Hicks, B. B.: The particle dry deposition component of total deposition from air quality models: right, wrong or uncertain?, 71, 1550324, https://doi.org/10.1080/16000889.2018.1550324, 2019.

Seinfeld, J. H. and Pandis, S. N.: Dry Deposition, in: Atmospheric Chemistry and Physics: From Air Pollution to 970 Climate Change, John Wiley & Sons, Inc., New York, NY, 1998.

Skov, K. R., Kolb, T. E., and Wallin, K. F.: Tree Size and Drought Affect Ponderosa Pine Physiological Response to Thinning and Burning Treatments, Forest Science, 50, 81–91, https://doi.org/10.1093/forestscience/50.1.81, 2004.

Slinn, S. A. and Slinn, W. G. N.: Predictions for particle deposition on natural waters, Atmospheric Environment (1967), 14, 1013–1016, https://doi.org/10.1016/0004-6981(80)90032-3, 1980.

975 Slinn, W. G. N.: Predictions for particle deposition to vegetative canopies, Atmospheric Environment (1967), 16, 1785–1794, https://doi.org/10.1016/0004-6981(82)90271-2, 1982.

Suni, T., Rinne, J., Reissell, A., Altimir, N., Keronen, P., Rannik, Ü., Dal Maso, M., Kulmala, M., and Vesala, T.: Long-term measurements of surface fluxes above a Scots pine forest in Hyytiälä, southern Finland, 1996-2001, Boreal Env. Res., 8, 287–301, 2003.

980 Tammet, H., Kimmel, V., and Israelsson, S.: Effect of atmospheric electricity on dry deposition of airborne particles from atmosphere, Atmospheric Environment, 35, 3413–3419, https://doi.org/10.1016/S1352-2310(01)00119-4, 2001.

Thimijan, R. W. and Heins, R. D.: Photometric, radiometric, and quantum light units of measure: a review of procedures for interconversion, HortScience, 18, 818–822, 1983.

985 Von der Weiden, S. L., Drewnick, F., and Borrmann, S.: Particle Loss Calculator – a new software tool for the assessment of the performance of aerosol inlet systems, 2, 479–494, https://doi.org/10.5194/amt-2-479-2009, 2009.

Vong, R. J., Vong, I. J., Vickers, D., and Covert, D. S.: Size-dependent aerosol deposition velocities during BEARPEX'07, 10, 5749–5758, https://doi.org/10.5194/acp-10-5749-2010, 2010.

Waraghai, A. and Gravenhorst, G.: Dry Deposition of Atmosheric Particles to an Old Spruce Stand, in: 990 Mechanisms and Effects of Pollutant-Transfer into Forests: Proceedings of the Meeting on Mechanisms and Effects of Pollutant-Transfer into Forests, held in Oberursel/Taunus, F.R.G., November 24–25, 1988, edited by: Georgii, H.-W., Springer Netherlands, Dordrecht, 77–86, https://doi.org/10.1007/978-94-009-1023-2_9, 1989.

Wilczak, J. M., Oncley, S. P., and Stage, S. A.: Sonic Anemometer Tilt Correction Algorithms, Boundary-Layer Meteorology, 99, 127–150, https://doi.org/10.1023/A:1018966204465, 2001.

Atmospheric
Chemistry
and Physics
Discussions

995   Zha, Y., Shi, Y., Tang, J., Liu, X., Feng, C., and Zhang, Y.: Spatial-Temporal Variability and Dust-Capture
       Capability of 8 Plants in Urban China, Pol. J. Environ. Stud., 28, 453–462, https://doi.org/10.15244/pjoes/81679,
       2018.

       Zhai, J., Cong, L., Yan, G., Wu, Y., Liu, J., Wang, Y., Ma, W., and Zhang, Z.: Dry Deposition of Particulate Matter
       and Ions in Forest at Different Heights, Int J Environ Res, 13, 117–130, https://doi.org/10.1007/s41742-018-0158-z,
1000   2019.

       Zhang, J., Shao, Y., and Huang, N.: Measurements of dust deposition velocity in a wind-tunnel experiment, 14,
       8869–8882, https://doi.org/10.5194/acp-14-8869-2014, 2014.

       Zhang, J. W., Feng, Z., Cregg, B. M., and Schumann, C. M.: Carbon isotopic composition, gas exchange, and
       growth of three populations of ponderosa pine differing in drought tolerance, Tree Physiology, 17, 461–466,
1005   https://doi.org/10.1093/treephys/17.7.461, 1997.

       Zhang, L., Gong, S., Padro, J., and Barrie, L.: A size-segregated particle dry deposition scheme for an atmospheric
       aerosol module, Atmospheric Environment, 35, 549–560, https://doi.org/10.1016/S1352-2310(00)00326-5, 2001.

       Zhang, Z., Liu, J., Wu, Y., Yan, G., Zhu, L., and Yu, X.: Multi-scale comparison of the fine particle removal
       capacity of urban forests and wetlands, Sci Rep, 7, 46214, https://doi.org/10.1038/srep46214, 2017.

1010